TECHNISCHE MECHANIK, Band 29, Heft 1, (2009), 60 - 85
Manuskripteingang: 25. August 2008

High-Frequency Self-Excitation in Paper Calenders

E. Brommundt

High-frequency self-oscillations can occur in paper calenders due to the compression of the paper in the nip together with the friction between paper and cylindrical rolls. Wear will follow and corrugate the rolls. This article elaborates a model demonstrating this effect and gaining insight into some details of the mechanism. The model parameters are chosen rather roughly so that the numerical values of the results will have little practical relevance. But the model uncovers parameters which, when changed, stabilize or destabilize the system. These tendencies might be compared with observations at machines to check the model.

1 Introduction

For printability, the surface of paper is finished by calendering: the paper sheet passes through the nip between two rolls where the web is compressed and its surface smoothened. Often, after an operating period of one or two weeks, barring occurs: waves develop on the surface of the rolls. This non-circularity generates wavy patterns on the paper, the bars. Because of the insufficient quality of such paper and the generated noise the machine must be shut down.

Self-excitation due to various time delays contained in the roll system in combination with regenerative wear seem to feed the deteriorating process (see Hader 2005, or Shelley et al. 1997 and the literature quoted there). Here, we assume that wear need not be the triggering effect. It is possible that there exists the combination of two processes: The first one is a friction induced self-excitation which can emerge even in a mill with ideally cylindrical rolls, to be shown below. That this is the case, the self-excited oscillation will produce corrugation by wear which, secondly, amplified by regeneration, may eventually govern the process.

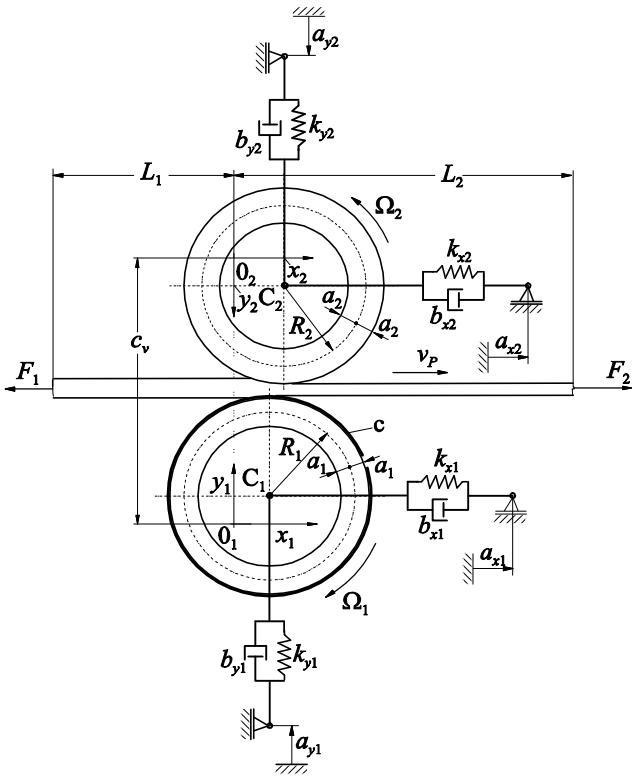

Figure 1: The system. Dimensions of the rolls and displacements of their centers

A preceding model of a very simple system with a single roll showed a high-frequency self-excitation (Brommundt, 2007). The mechanism there bases on friction between paper and roll and on the dissipation during the compression of a linear visco-elastic paper at a small prescribed (macro) slip.

The present model comprises two rolls, the lower one is driven by an external drive via a flexible clutch, the upper one is driven from below by friction in the nip. The deformations of the rolls and their suspensions are modeled in some detail. (The cover of the lower roll is disregarded.) For the paper compression holds a nonlinear hysteretic characteristic, modified by a viscous damping. The slip between rolls and paper is not prescribed but follows from the dynamic equilibrium conditions in the nip, taking Coulomb friction into account. For the relatively large coefficients of friction chosen the macro slip is tiny, the signs of the relative velocities between paper and rolls change twice along the passage of the paper through the nip.

2 The Model

2.1 Outline of the System

A brief description of the rolling processes of paper is given in the introduction of van Haag (1993), roller details can be found in Roisum (1996). Figure 1 shows our model: A paper sheet, or web, runs continuously through the nip between two rolls. The sheet enters the model from the left, tightened by a tension force F_1 and leaves it at the right, where the tension force F_2 acts. Both forces are assumed to be kept stationary at prescribed values by suitably controlled rolls (not shown in the Figure), placed at the distances L_1, L_2 with respect to the vertical reference line through the origins 0_1, 0_2 of the Cartesian coordinate systems $(0_1,x_1,y_1)$, $(0_2, x_2, y_2)$, which are mirror images of each other with respect to the paper surface. The rolls are long cylindrical shells. Bending about their axes as well as the longitudinal deformation will be neglected. Thus, we are dealing with plane strain and can regard the rolls as elastic rings (subscripts 1 for the lower ring, subscripts 2 for the upper one). However, to be allowed to look upon loads as forces or moments – and not as load/length-quantities – we assume a width of $b = 1$ m in the cross direction of the paper sheet. At their nominal centers C_1, C_2 the rolls are kept by preloaded visco-elastic suspensions (the quantities a_{x1}, a_{y1}, a_{x2}, a_{y2} serve for adjustments). A motor, running with a constant (nominal) angular velocity Ω_N is coupled visco-elastically to the lower roll (whose flexible cover c is neglected here, to simplify matters). Depending on the normal pressure and the ensuing relative velocity between roll surface and paper, distributed along the nip, the lower roll exerts a longitudinal friction force on the paper, in general (certainly if $F_1 > F_2$) it will pull. Conversely, the upper roll, driven from below by friction but impeded by a retarding moment M_r, will adjust its angular velocity corresponding to the kinematical and dynamical conditions.

In the system meet high frequency machine dynamics – which determines approximately linear vibration frequencies and modes – and strictly nonlinear interactions at the nip – which govern the energy exchanges between drive and oscillations, determine their time dependent magnitudes and the relative amplitudes of the (linear) modes.

Because of the high frequencies, deformations of the cylindrical rolls (the circular rings) are taken into account but the corresponding parts of the equations of motion are kept linear. The model of the elastic rings in Appendix 1 allows for extension $u(\psi,t)$ in the circumferential direction, bending $w(\psi,t)$ like a curved beam, and shear deformation $v(\psi,t)$, cf. Figure A.1.1. Appendix 1 establishes the basic model of the roll displacements and deformations. Appendix 2 list the resulting linear terms of the equations of motion, their machine dynamics part, in the form they get after the discretization of Sect. 2.2.

At the nip, the contact zone, the quantities describing the details of the paper compression, and of the kinematical, frictional and dynamical processes are of widely differing magnitudes. Sect. 3 explores these magnitudes on the basis of the roll displacements and deformations (Appendixes 1 and 2) and develops a rather complex nonlinear model, suitably detailed, discretized and simplified, which determines the dynamic coupling between rolls and paper and rules the energy exchange in the equations of motion.

2.2 Discretization

The equations of motion will be established by Hamilton's Principle:

$$\int_{t_1}^{t_2} \left(\delta T - \delta U + \delta W \right) \mathrm{d}t = 0, \tag{2.1}$$

where T – kinetic energy, U – potential, and δW is the virtual work of the forces not contained in the potential. Appendix A.1 elaborates for the deformations of the rolls, $u(\psi,t)$, $v(\psi,t)$, $w(\psi,t)$, the displaced hubs and the suspensions the pertinent terms of potential and kinetic energy. Parts of the virtual work are given there, parts follow in Sect. 3.

Since the rolls and the paper are continuous media, partial differential equations (PDEs) govern their motions. To avoid the difficulties of the solution of PDEs, we discretize the system and introduce (discrete) generalized coordinates $q_k(t)$, $k = 1,...,48$, in the following way:

At the lower roll, i.e. roll 1, cf. Figure 1, we have the displacements of the axis,

$$x_1(t) = q_1,\ y_1(t) = q_2, \tag{2.2}$$

and for the deformations $u_1(\psi_1,t)$, $v_1(\psi_1,t)$, $w_1(\psi_1,t)$ hold the discretizations

$$\begin{aligned} u_1(\psi_1,t) &= q_3 + q_4\cos(\psi_1) + q_5\sin(\psi_1) + q_6\cos(2\psi_1) + q_7\sin(2\psi_1) + q_8\cos(3\psi_1) + q_9\sin(3\psi_1), \\ v_1(\psi_1,t) &= q_{10} + q_{11}\cos(\psi_1) + q_{12}\sin(\psi_1) + q_{13}\cos(2\psi_1) + q_{14}\sin(2\psi_1) + q_{15}\cos(3\psi_1) + q_{16}\sin(3\psi_1), \\ w_1(\psi_1,t) &= q_{17} + q_{18}\cos(\psi_1) + q_{19}\sin(\psi_1) + q_{20}\cos(2\psi_1) + q_{21}\sin(2\psi_1) + q_{22}\cos(3\psi_1) + q_{23}\sin(3\psi_1). \end{aligned} \tag{2.3}$$

The angular velocity $\Omega_1(t)$ of the lower roll (mean value about the circumference) is given by

$$\Omega_1 = \Omega_N + \dot{\Phi}_m = \Omega_N + \dot{q}_3/R_1, \tag{2.4}$$

where Ω_N is the nominal angular velocity of the drive.

At the upper roll, i.e. roll 2, cf. Figure 1, we have the rotation and the displacements of the hub,

$$\Phi_2(t)\cdot R_2 = q_{24},\ x_2(t) = q_{25},\ y_2(t) = q_{26}, \tag{2.5}$$

and for the deformations $u_2(\psi_2,t)$, $v_2(\psi_2,t)$, $w_2(\psi_2,t)$ hold the discretizations

$$\begin{aligned} u_2(\psi_2,t) &= q_{27} + q_{28}\cos(\psi_2) + q_{29}\sin(\psi_2) + q_{30}\cos(2\psi_2) + q_{31}\sin(2\psi_2) + q_{32}\cos(3\psi_2) + q_{33}\sin(3\psi_2), \\ v_2(\psi_2,t) &= q_{34} + q_{35}\cos(\psi_2) + q_{36}\sin(\psi_2) + q_{37}\cos(2\psi_2) + q_{38}\sin(2\psi_2) + q_{39}\cos(3\psi_2) + q_{40}\sin(3\psi_2), \\ w_2(\psi_2,t) &= q_{41} + q_{42}\cos(\psi_2) + q_{43}\sin(\psi_2) + q_{44}\cos(2\psi_2) + q_{45}\sin(2\psi_2) + q_{46}\cos(3\psi_2) + q_{47}\sin(3\psi_2). \end{aligned} \tag{2.6}$$

The angular velocity $\Omega_2(t)$ of the upper roll is given by (cf. $(2.5)_1$, Figure 1 and FigurA.1.3):

$$\Omega_2 = \dot{\Phi}_2 = \dot{q}_{24}/R_2. \tag{2.7}$$

The last coordinate, $q_{48}(t)$, measures the motion $x_P(t)$ of the paper in the machine direction, respectively its velocity $v_P(t)$, see Figure 1:

$$x_P(t) = q_{48},\ v_P(t) = \dot{q}_{48}. \tag{2.8}$$

The generalized coordinates $q_k(t)$ are assembled in the configuration vectors (column matrices)

$$\mathbf{q}_1 := (q_1,...,q_{23})^T,\ \mathbf{q}_2 := (q_{24},...,q_{47})^T,\ \mathbf{q} = (\mathbf{q}_1^T, \mathbf{q}_2^T, q_{48})^T, \tag{2.9}$$

related to the lower roll, the upper roll and the system as a whole, respectively.

2.3 The Structure of the Equations of Motion

For the generalized coordinates $q_k(t)$ follow from Hamilton's Principle the Lagrangian Equations

$$\frac{\mathrm{d}}{\mathrm{d}t}\left(\frac{\partial T}{\partial \dot{q}_k}\right) - \frac{\partial T}{\partial q_k} + \frac{\partial U}{\partial \dot{q}_k} = Q_k,\ k = 1,...,48, \tag{2.10}$$

where the generalized forces $Q_k(t)$ are assembled in the force vectors

$$\mathbf{Q}_1 := (Q_1,...,Q_{23})^T,\ \mathbf{Q}_2 := (Q_{24},...,Q_{47})^T,\ \mathbf{Q} = (\mathbf{Q}_1^T, \mathbf{Q}_2^T, Q_{48})^T, \tag{2.12}$$

to be calculated from the virtual work δW by

$$\delta W = \sum_{k=1}^{48} Q_k \, \delta q_k . \tag{2.13}$$

2.3 The Equations of Motion

The equations of motion, obtained by (2.10), get the form

$$\mathbf{M}\,\ddot{\mathbf{q}} + \boldsymbol{\Omega}\,\mathbf{G}\,\dot{\mathbf{q}} + \boldsymbol{\Omega}^2\,\mathbf{C}\,\mathbf{q} + \mathbf{B}\,\dot{\mathbf{q}} + \boldsymbol{\Omega}\,\mathbf{B}^r\mathbf{q} + \mathbf{K}\,\mathbf{q} = \mathbf{A}\,\mathbf{a} + \mathbf{f}_w + \mathbf{f}_c . \tag{2.14}$$

The left-hand side and the terms $\mathbf{A}\ \mathbf{a} + \mathbf{f}_w$ on the right represent the machine dynamic part of the problem, prepared in Appendix 2 and to be incorporated below. The contact forces $\mathbf{f}_c$, acting in the nip, will be established in Sect. 3.

Parallel to the structure $(2.9)_3$ of the configuration vector $\mathbf{q}$ the matrices of (2.14) get the block-diagonal forms

$$\begin{aligned}
&\mathbf{M} = \begin{pmatrix} \mathbf{M}_{11} & & \\ & \mathbf{M}_{22} & \\ & & m_P \end{pmatrix}, \mathbf{G} = \begin{pmatrix} \mathbf{G}_{11} & & \\ & \mathbf{G}_{22} & \\ & & 0 \end{pmatrix}, \mathbf{C} = \begin{pmatrix} \mathbf{C}_{11} & & \\ & \mathbf{C}_{22} & \\ & & 0 \end{pmatrix}, \quad \mathbf{B} = \begin{pmatrix} \mathbf{B}_{11} & & \\ & \mathbf{B}_{22} & \\ & & 0 \end{pmatrix}, \\
&\mathbf{B}^r = \begin{pmatrix} \mathbf{0} & & \\ & \mathbf{B}^r_{22} & \\ & & 0 \end{pmatrix}, \qquad \mathbf{K} = \begin{pmatrix} \mathbf{K}_{11} & & \\ & \mathbf{K}_{22} & \\ & & 0 \end{pmatrix}, \boldsymbol{\Omega} = \begin{pmatrix} \Omega_1 \mathbf{I}_{11} & & \\ & \Omega_2 \mathbf{I}_{22} & \\ & & 0 \end{pmatrix},
\end{aligned} \tag{2.15}$$

with zeroes outside the diagonals, and $\mathbf{I}_{11}$, $\mathbf{I}_{22}$ are unit matrices of 23×23 and 24×24 elements, respectively. The matrices $\mathbf{M}_{11}$, $\mathbf{G}_{11}$, etc. as well as $\mathbf{M}_{22}$, $\mathbf{G}_{22}$, etc. are the sums of the relevant matrices of the Appendixes A.2.2 – A.2.4, containing the numerical values of the parameters belonging to the lower and the upper roll, respectively. (To get 23×23-matrices $\mathbf{M}_{11}$, $\mathbf{G}_{11}$, etc. from the matrices of Appendix 2, the first columns and rows must be cancelled.) The inertia m_P is the mass of the paper sheet, width $b = 1\,\mathrm{m}$, length $(L_1 + L_2)$ see Figure 1.

The 'static forces' on the right-hand side are separated: $\mathbf{A}\ \mathbf{a}$ expresses the effects of the adjustments

$$\mathbf{a} = (a_{x1}, a_{y1}, R_1\varphi_{n0}, a_{S1}, a_{S2}, a_{S3}, a_{x2}, a_{y2}, F_1, F_2, M_r)^T, \text{where } a_{Sl} = -F_{Sl}/k_{Sl}, \tag{2.16}$$

which, together, determine the working positions of the rolls and must be chosen appropriately; see (A.2.14) for the matrix $\mathbf{A}$; the column $\mathbf{f}_w$ contains the forces from the weights, see (A.2.15).

3 The Contact Zone

3.1 Geometric and Kinematical Relations at the Nip

The study of the deformations and forces at the nip requires some series expansions for which we need to know the magnitudes of the geometric quantities involved. From Figure 2 we read for rigid rolls in idealized position for given outer radii R_{o1}, Ro_2, paper thicknesses H_1, H_N at the entrance point and the narrowest point, respectively:

$$\begin{aligned}
&h_{1o} = R_{o1}(1-\cos\psi_{1o}),\ h_{2o} = R_{o2}(1-\cos\psi_{2o}),\ \Delta H = H_1 - H_N, \\
&\Delta H_o = h_{1o} + h_{2o},\ \ l_1 = R_{o1}\sin\psi_{1o} = R_{o2}\sin\psi_{2o}.
\end{aligned} \tag{3.1}$$

One Taylor term of the sin- and two of the cos-functions lead to the length of the compressive section of the nip

$$l_1 = \sqrt{2\,\Delta H_o\,\bar{R}},\ \text{where } \bar{R} = R_{o1}R_{o2}/(R_{o1}+R_{o2}). \tag{3.2}$$

With $Ro1$ = 486 mm, R_{o2} = 346 mm, H_1 = 0.15 mm, H_N = 0.07 mm, cf. Sect. 4.4, Figure 7, follow

$$R_{o1} : l_1 : \Delta H_o : \hat{q} \approx 346 : 5.32 : 0.07 : 0.002 \approx 1 : \varepsilon : \varepsilon^2 : \varepsilon^3, \tag{3.3}$$

where $\hat{q} = 0.002$ mm is a magnitude of the vibration amplitudes expected and $\varepsilon \approx 1/50$.

Figure 3 presents the geometrical relations at the nip of the deformable rolls. The large paper offset, apparent between entrance and exit in the vertical direction, is due mostly to the exaggerated thickness of the paper sheet and the diminished roll radii as drawn for the perceptibility of the details

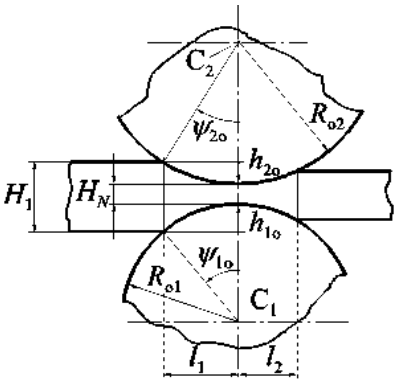

Figure 2: Shape of the nip of two rigid rolls in idealized position

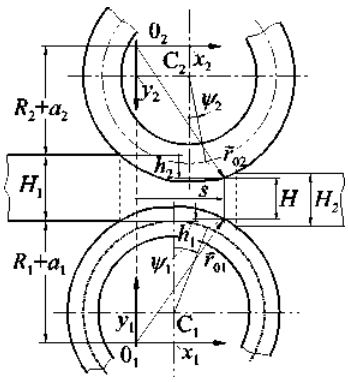

Figure 3: Geometric relations at the nip of flexible rolls

Let the origins 0_1, 0_2 of the two coordinate systems (0_1, x_1, y_1), (0_2, x_2, y_2), lie on the vertical line, dashed in the figure. From the line counts the horizontal coordinate s along the nip. Throughout the following investigations, let the adjustments ax_1, ax_2, see Figure 1, be chosen such that the horizontal displacements x_1, x_2 of the roll centers C_1, C_2 are small enough to allow to assume that the nip lies horizontally, and that the paper arrives at and leaves contact with the rolls at its lower and its upper surface simultaneously, that the instantaneous compression forces are functions of (s,t). (Of course, these assumptions imply restrictions on the accuracy of the investigation which will not be detailed here.)

We look for a presentation of the shape of the compressed paper in the nip region as function of (s,t):

$$H(s,t) = H_1 - h_1(s,t) - h_2(s,t), \tag{3.4}$$

see Figure 3. By that Figure follows from (A.1.20) for the upper roll at the instant t, (subscripts 2 not written),

$$\begin{aligned} &s\,\vec{e}_x + (R+a+h)\,\vec{e}_y = x(t)\,\vec{e}_x + y(t)\,\vec{e}_y + \vec{r}(\psi,a,t), \text{ decomposed:} \\ &s = x(t) + \vec{e}_x \cdot \vec{r}(\psi,a,t),\ (R+a+h) = y(t) + \vec{e}_y \cdot \vec{r}(\psi,a,t). \end{aligned} \tag{3.5}$$

For a (numerically) given configuration vector $\mathbf{q} = \mathbf{q}(t)$, with 24 elements, and with (A.1.8), (A.2.1) the relations of the second line are expanded with respect to ψ. According to (3.3) hold

$$(R,a,x,s,\psi,y,h,\mathbf{q}) => (R,a,\varepsilon\,x,\varepsilon\,s,\varepsilon\,\psi,\varepsilon^2 y,\varepsilon^2 h,\varepsilon^3\mathbf{q}), \tag{3.6}$$

Up to the order ε^3 the expansions read, after division by ε and ε^3 of the first and the second relation, respectively:

$$\begin{aligned} s &= x + (R+a)\psi - (R+a)\varepsilon^2\psi^3/6 + \varepsilon^2 \mathbf{s}_{20}\mathbf{q} + \varepsilon^3\psi\,\mathbf{s}_{31}\mathbf{q}, \\ h &= y - (R+a)\psi^2/2 + \varepsilon\,\mathbf{h}_{10}\mathbf{q} + \varepsilon^2\psi\ \mathbf{h}_{21}\mathbf{q} + (R+a)\varepsilon^2\psi^4/24. \end{aligned} \tag{3.7}$$

The row matrices $\mathbf{s}_{jk}$, $\mathbf{h}_{jk}$, multiplied by $\varepsilon^j\,\psi^k$ and $\mathbf{q}$ as shown, are listed in (A.3.1) to (A.3.4) of Appendix. A.3.

In a similar way follow for the material velocity $\mathbf{v} = \vec{e}_x v_x + \vec{e}_y v_y$ of the point on the roll surface, located instantaneously at (ψ, a), from (A.1.24), (A.1.26)

$$
\begin{aligned}
v_x = \quad & \dot{x} + \Omega(R+a) + \varepsilon^2 \mathbf{v}_{x20}\,\dot{\mathbf{q}} - \Omega(R+a)\,\varepsilon^2\psi^2/2 + \varepsilon^3\,\Omega\,\mathbf{v}_{x30}\,\mathbf{q} + \varepsilon^3\psi\,\mathbf{v}_{x31}\,\dot{\mathbf{q}}, \\
v_y = \quad & \dot{y} - \Omega(R+a)\psi + \varepsilon\,\mathbf{v}_{y10}\,\dot{\mathbf{q}} + \varepsilon^2\,\Omega\,\mathbf{v}_{y20}\,\mathbf{q} + \varepsilon^2\psi\,\mathbf{v}_{y21}\,\dot{\mathbf{q}} + \Omega(R+a)\,\varepsilon^2\psi^3/6 \\
& + \varepsilon^3\psi\,\Omega\,\mathbf{v}_{y31}\,\mathbf{q} + \varepsilon^3\psi^2\,\mathbf{v}_{y32}\,\dot{\mathbf{q}},
\end{aligned}
\tag{3.8}
$$

where the high frequencies of the vibrations are assumed to have a magnitude of Ω_N/ε. Consequently, $\dot{y}, \dot{\mathbf{q}}$ enter the expansion as $\varepsilon\dot{y}, \varepsilon^2\dot{\mathbf{q}}$, but the expansion of v_y is divided by ε. The row matrices $\mathbf{v}_{xjk}$, $\mathbf{v}_{yjk}$ are listed in (A.3.5) to (A.3.8). (In (3.8) and (3.9), the first three elements of $\mathbf{q}$ and $\delta\mathbf{q}$ respectively, are extracted from the matrix notation and placed separately.)

The expansion of the virtual displacement $\delta\vec{r}_{0a} =: \delta s\,\vec{e}_x + \delta h\,\vec{e}_y$, at the point $\zeta = a$, cf.$(A.1.28)_1$, is

$$
\begin{aligned}
\delta s &= \delta x + (1+\tilde{a})(1-\varepsilon^2\psi^2/2)\,\delta q_1 + \mathbf{k}_{x00}\,\delta\mathbf{q} + \varepsilon\psi\,\mathbf{k}_{x11}\,\delta\mathbf{q} + \varepsilon^2\psi^2\mathbf{k}_{x22}\,\delta\mathbf{q}, \\
\delta h &= \delta y - (1+\tilde{a})\,\delta q_1 \qquad\qquad + \mathbf{k}_{y00}\,\delta\mathbf{q} + \varepsilon\psi\,\mathbf{k}_{y11}\,\delta\mathbf{q} + \varepsilon^2\psi^2\mathbf{k}_{y22}\,\delta\mathbf{q}.
\end{aligned}
\tag{3.9}
$$

The row matrices $\mathbf{k}_{xiy}$, $\mathbf{k}_{yij}$ are listed in (A.3.9) to (A.3.11).

For given $\mathbf{q} = \mathbf{q}(t)$ follows from $(3.7)_1$ by inversion the angle ψ related to the material point on the surface of the roll (ring) which is instantaneously – at the time t – at s. This angle is put into the relations $(3.7)_2$ to (3.9) to obtain the pertinent values of h, v_x, v_y, δs, δh. Up to second order terms of ε hold

$$
\psi = (s-x)/(R+a) + \varepsilon^2/6\,\big((s-x)/(R+a)\big)^3 - \varepsilon^2\mathbf{s}_{20}\,\mathbf{q}/(R+a),
\tag{3.10}
$$

$$
h = y - (s-x)^2/2(R+a) + \varepsilon\,\mathbf{h}_{10}\,\mathbf{q} - \varepsilon^2(s-x)/8(R+a)^3\cdot\Big((s-x)^3 - 8(R+a)^2(\mathbf{h}_{21}+\mathbf{s}_{20})\,\mathbf{q}\Big),
\tag{3.11}
$$

$$
\begin{aligned}
v_x &= \dot{x} + \Omega(R+a) - \varepsilon^2\,\Omega(s-x)^2/2(R+a) + \varepsilon^2\,\mathbf{v}_{x20}\,\dot{\mathbf{q}}, \\
v_y &= \dot{y} - \Omega(s-x) + \varepsilon\,\mathbf{v}_{y10}\,\dot{\mathbf{q}} + \varepsilon^2\,\Omega(\mathbf{s}_{20}+\mathbf{v}_{y20})\,\mathbf{q} + \varepsilon^2\,(s-x)\,\mathbf{v}_{y21}\,\dot{\mathbf{q}}/(R+a),
\end{aligned}
\tag{3.12}
$$

$$
\begin{aligned}
\delta s &= \delta x + \mathbf{k}_{x00}\,\delta\mathbf{q} + (1+\tilde{a})\,\delta q_1 + \frac{\varepsilon(s-x)\,\mathbf{k}_{x11}\,\delta\mathbf{q}}{(R+a)} + \varepsilon^2(s-x)^2\,\frac{2\,\mathbf{k}_{x22}\,\delta\mathbf{q} - (1+\tilde{a})\,\delta q_1}{2(R+a)^2}, \\
\delta h &= \delta y + \mathbf{k}_{y00}\,\delta\mathbf{q} + \varepsilon(s-x)\,\frac{\mathbf{k}_{y11}\,\delta\mathbf{q} - (1+\tilde{a})\,\delta q_1}{(R+a)} + \varepsilon^2(s-x)^2\,\frac{\mathbf{k}_{y22}\,\delta\mathbf{q}}{(R+a)^2}.
\end{aligned}
\tag{3.13}
$$

3.2 Paper Compression

For the compression of the paper we take the phenomenological model of Hader (see Hader 2005, Sect.5, and the literature quoted there). Let $\sigma_p(s,t)$, $\varepsilon_p(s,t)$ be the stress and strain normal to the sheet of the paper (compression positive; small subscripts p). The paper is free of normal stress and strain when it enters the nip, at $s = s_1(t)$, $s_1 < 0$, to be determined below from

$$
\varepsilon_p(s_1, t) = 0.
\tag{3.14}
$$

Due to the narrowing nip the paper is loaded and compressed up to maximal values σ_m, ε_m at the (instantaneously) narrowest gap. Afterward, running through the widening section of the nip it is unloaded till

$$
\sigma_p(s_2, t) = 0,
\tag{3.15}
$$

which determines $s_2 = s_2(t)$. Because of a remanent (plastic) deformation the paper will not recover completely, there remains a residual strain $\varepsilon_r(t) = \varepsilon_p(s_2,t) > 0$, cf. Figure 4.

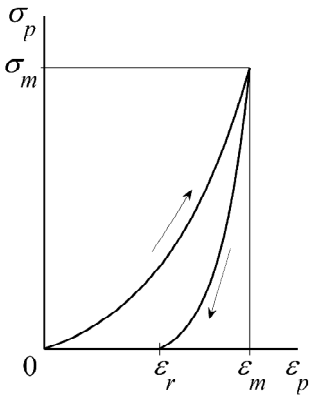

Figure 4: Stress-strain relation for paper compression

For the loading and the unloading branch of $\sigma_p(\varepsilon_p)$ in Figure 4 hold

$$\begin{aligned} \sigma_{pl}(\varepsilon_p) &= E_l\,\varepsilon_l \cdot \left(\exp(\varepsilon_p/\varepsilon_l)-1\right), \\ \sigma_{pul}(\varepsilon_p) &= E_{ul}\,\varepsilon_{ul} \cdot \left(\exp((\varepsilon_p-\varepsilon_r)/\varepsilon_{ul})-1\right), \end{aligned} \tag{3.16}$$

parameters are E_l, E_{ul} ($> E_l$), the moduli of elasticity at $\sigma_p = 0$, for ε_l, ε_{ul}, respectively. The residual strain σ_r is calculated, for given ε_m, from the condition

$$\sigma_{pl}(\varepsilon_m) = \sigma_{pul}(\varepsilon_m). \tag{3.17}$$

Because of the high frequency oscillations, the sign of ε_p at a material point of the paper might invert several times when passing the nip. Then the stress process $\sigma_p(\varepsilon_p)$ should be put together of corresponding loading and unloading pieces of (3.16). Since the high frequency parts of the oscillations have very small amplitudes we avoid the corresponding cumbersome calculations and take below just one change of the sign into account. Likewise neglected is the influence of the longitudinal deformation of the paper sheet on the normal stresses and strains (in calendering that deformation is considered to be negligibly small).

On the other hand, in the high frequency system, the velocity of the loading will have an effect on the stresses in the nip. To avoid complications, especially not to spoil the condition (3.14), let the stress $\sigma_P(\varepsilon_p, \dot{\varepsilon}_P)$ which comprises the dependence on the strain ε_p and on its material time derivative $\dot{\varepsilon}_P$ be given by

$$\sigma_P = \sigma_P(\varepsilon_p, \dot{\varepsilon}_P) = \sigma_p(\varepsilon_p) \cdot \exp(b_p\,\dot{\varepsilon}_P), \tag{3.18}$$

where $\sigma_p(\varepsilon_p)$ is the stress known from (3.16), and b_p is a damping coefficient of dimension time (distinguish the subscripts small p and large P). To get some insight into this relation, we take in (3.18), for small $|\,b_p\,\dot{\varepsilon}_P\,|$, the first two terms of the exponential series:

$$\sigma_P = \sigma_p(\varepsilon_p) + \sigma_p(\varepsilon_p) \cdot (b_p\,\dot{\varepsilon}_P). \tag{3.19}$$

In this approximation, the original stress $\sigma_p(\varepsilon_p)$ and the 'viscous stress' $\sigma_p(\varepsilon_p) \cdot (b_p\,\dot{\varepsilon}_P)$ look like acting in parallel, similar as the suspension devices in Figure 1.

3.3 Forces due to Paper Compression

The forces calculated here enter in Sect. 3.4 the right-hand side of the differential equation (2.14), meaning that, at the instant t, the configuration vector $\mathbf{q}$, i.e. $\mathbf{q}_1$, $\mathbf{q}_2$, as well as the velocities $\dot{\mathbf{q}}$ are known numerically. Thus, all quantities (3.10) to (3.13) and, as far as required, their derivatives can be computed.

From (3.11) we obtain $h_1(s,t)$, $h_2(s,t)$ and

$$\begin{aligned} h_s &= h_1 + h_2 = y_1 + y_2 - (s-x_1)^2/2(R_1+a_1) - (s-x_2)^2/2(R_2+a_2) + \varepsilon \cdot \left(h_{1res} + h_{2res}\right), \\ h_s' &= \delta h_s/\delta s = -(s-x_1)/(R_1+a_1) - (s-x_2)/(R_2+a_2) + \varepsilon \cdot \left(h_{1res}' + h_{2res}'\right), \\ \dot{h}_s &= \delta h_s/\delta t = \dot{y}_1 + \dot{y}_2 + \dot{x}_1\,(s-x_1)/(R_1+a_1) + \dot{x}_2\,(s-x_2)/(R_2+a_2) + \varepsilon \cdot \left(\dot{h}_{1res} + \dot{h}_{2res}\right), \end{aligned} \tag{3.20}$$

where $\varepsilon \cdot (h_{1res} + h_{2res})$ comprises the terms of order ε and ε^2. Figure 3 shows

$$\varepsilon_p(s,t) = h_s(s,t)/H_1\,. \tag{3.21}$$

From $(3.12)_2$ follow $v_{y1}(s,t)$, $v_{y2}(s,t)$ and $\dot{\varepsilon}_P$, the material time derivative of the paper strain is given by

$$\dot{\varepsilon}_P(s,t) = \left(\delta h_s/\delta t + v_P\,\delta h_s/\delta s\right)\Big/H_1 = \left(\dot{h}_s + v_P\,h_s'\right)\Big/H_1\,, \tag{3.22}$$

where $v_P = \dot{q}_{48}$ is the velocity of the paper, cf. $(2.8)_2$ and Figure 1. With $\varepsilon_p, \dot{\varepsilon}_P$ known, the stresses can be computed by $(3.16)_1$ and (3.18) for the narrowing part of the nip. The strain ε_p attains its maximum at $s = s_N$, $\varepsilon_m = \varepsilon_p(s_N,t)$, and s_N is obtained from $h_s'(s_N,t) = 0$, cf. $(3.20)_2$, by recursion.

To evaluate $(3.16)_2$, for a point of the paper presently at $s > s_N$, in the widening part of the nip, we need the maximal compression $\varepsilon_m(s,t)$ it underwent before. (A recording which moves along with the paper sheet would be best but requires much computational effort.) To simplify matters, we take as maximal compression the present value $\varepsilon_m = \varepsilon_p(s_N,t)$, calculate σ_m by $(3.16)_1$, put it into $(3.16)_2$ and solve for ε_r:

$$\varepsilon_r = \varepsilon_m - \varepsilon_{ul}\ln\left(E_l\,\varepsilon_l/E_{ul}\,\varepsilon_{ul}\cdot\left(\exp(\varepsilon_m/\varepsilon_l)-1\right)+1\right). \tag{3.23}$$

With ε_r known, $(3.16)_2$, (3.19) can be evaluated for $s > s_N$.

The borders s_1, s_2 of the instantaneous contact region $s_1 \le s \le s_2$ are computed in the following way: Condition (3.14) leads to $h_s(s_1,t) = 0$, and s_1 is obtained from $(3.20)_2$ by recursion. The condition (3.14) leads to $\varepsilon_p(s_2,t) = \varepsilon_r$, equivalent to $h_s(s_2,t) = \varepsilon_r H_1$, which is solved for s_2 by recursion again.

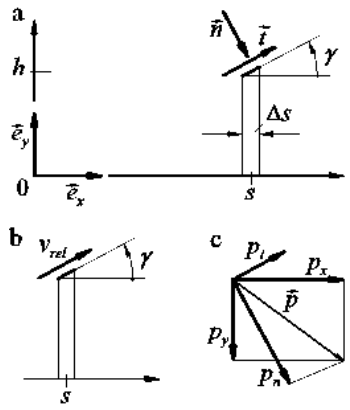

Figure 5: Point s, $h(s,t)$ on the surface of the lower roll. a) Directions, b) relative velocity, c) distributed load $\vec{p}$ and its decompositions

3.4 Forces acting between Roll and Paper

Figure 5 shows the situation at a point $[s, h(s,t)]$ on the surface of the lower roll. The figure defines the positive orientations of the quantities. (The subscripts 1 are written only when necessary for distinction. The normal and tangential vectors, $\vec{n}, \vec{t}$, must not be confused with those of (A.1.5). For the upper roll holds a mirror image of Figure 5, cf. the remark in Sect. 2.1.)

From Figure 5a and (3.11) it is seen:

$$\tan\gamma = h',\ \vec{n} = \vec{e}_x\sin\gamma - \vec{e}_y\cos\gamma,\ \vec{t} = \vec{e}_x\cos\gamma + \vec{e}_y\sin\gamma. \tag{3.24}$$

The material velocity at the surface of the roll follows by (3.12):

$$\vec{v}_1 = \vec{e}_x v_x + \vec{e}_y v_y. \tag{3.25}$$

The material velocity at the surface of the paper, bending neglected, is approximated by, cf. (3.22),

$$\vec{v}_p = \vec{e}_x v + \vec{e}_y(\dot{h} + v_P\,h'). \tag{3.26}$$

Then holds for the relative velocity v_{rel} of the material point of the paper with respect to the material point of the roll, presently at s cf. Figure 5b, the scalar product

$$v_{rel} = (\vec{v}_p - \vec{v}_1)\cdot\vec{t}\,. \tag{3.27}$$

The distributed load $\vec{p}$, see Figure 5c, is decomposed in two ways:

$$\vec{p} = \vec{e}_x p_x - \vec{e}_y p_y = \vec{n}\,p_n + \vec{t}\,p_t, \tag{3.28}$$

where the vertical component p_y is given by the product of the width b and the stress σ_P of (3.18):

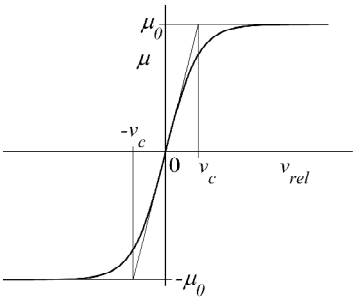

Figure 6: Coefficient of friction, $\mu = \mu(v_{rel})$

$$p_y = b\,\sigma_P. \tag{3.29}$$

The tangential component p_t is the product of μ, the coefficient of friction, and the normal component p_n:

$$p_t = \mu(v_{rel})\,p_n. \tag{3.30}$$

We assume for $\mu = \mu(v_{rel})$ a smoothened Coulomb characteristic (see Figure 6 and Brommundt 1995). An easily evaluated relation is

$$\mu = \mu_0 \tanh\left(v_{rel}/v_c\right), \tag{3.31}$$

where the corner velocity v_c is small: $0 < v_c \ll \Omega_N R$, see Figure 6. From the preceding equations and Figure 5c we obtain

$$p_x = \frac{\sin\gamma + \mu(v_{rel})\cos\gamma}{\cos\gamma - \mu(v_{rel})\sin\gamma}\,p_y. \tag{3.32}$$

Let the virtual displacement $\delta\vec{r}_{0a}$, (3.9), in vector form, be abbreviated by

$$\delta\vec{r}_{0a} = \delta\mathbf{q}^T\,\vec{\mathbf{k}}, \tag{3.33}$$

where, in contrast to (3.09), (3.13), $\delta\mathbf{q}$ and $\vec{\mathbf{k}}$ – the latter here a column matrix – contain also the terms of the rotation and the displacements x and y. Then we get the complete virtual work

$$\delta W = \delta\mathbf{q}_1^T \int_{s_1}^{s_2} \vec{\mathbf{k}}_1\cdot\vec{p}_1\,\mathrm{d}s + \delta\mathbf{q}_2^T \int_{s_1}^{s_2} \vec{\mathbf{k}}_2\cdot\vec{p}_2\,\mathrm{d}s - \delta q_{24}\,M_r - \delta q_{48}\int_{s_1}^{s_2}\left(\vec{p}_1+\vec{p}_2\right)\cdot\vec{e}_x\,\mathrm{d}s + \delta q_{48}\left(F_2 - F_1\right), \tag{3.34}$$

where s_1, s_2 are the instantaneous borders of the contact zone, cf. Sect. 3.3, the quantities with subscripts 1 applies for the lower roll, those with subscripts 2 for the upper one, M_r is a restraining moment applying on the upper roll, and the last two terms pertain to the paper.

4 Numerical Solutions to the Equations of Motion

4.1 The First Order System

For the numerical solution the equations (2.14) are transformed to the first order system

$$\dot{\mathbf{u}} = \mathbf{f}(\mathbf{u}), \tag{4.1}$$

where $\mathbf{u} := (\dot{\mathbf{q}}^T, \mathbf{q}^T)^T$ is the state vector and $\mathbf{f} := (\mathbf{f}_1^T, \mathbf{f}_2^T)^T$ is the corresponding right-hand side:

$$\mathbf{f}_1 = \mathbf{M}^{-1}\left(\mathbf{A}\,\mathbf{a} + \mathbf{f}_w + \mathbf{f}_c - \boldsymbol{\Omega}\,\mathbf{G}\,\dot{\mathbf{q}} - \boldsymbol{\Omega}^2\,\mathbf{C}\,\mathbf{q} - \mathbf{B}\,\dot{\mathbf{q}} - \boldsymbol{\Omega}\,\mathbf{B}^r\mathbf{q} - \mathbf{K}\,\mathbf{q}\right),\ \mathbf{f}_2 = \dot{\mathbf{q}}. \tag{4.2}$$

4.2 The System Parameters

The Tables A.4 to A.7 of Appendix A.4 list the 60 numerical values (rounded) of the system parameters. They are chosen, after some tentative numerical calculations, such that the practicability of the model turns out and some characteristics can be presented. Rough guiding lines for the overall dimensions of the machine followed

from discussions with experts of Voith Paper Company during a meeting at the Technical University Dresden (August 2006), and from the theses van Haag (1993), and Hader (2005). Stiffnesses were estimated by the choice of several lower natural frequencies (cf. Table 2 in Sect. 4.5.1). Of course, the adjustments a_x, a_y, see Figure 1, had to be adapted during the start of the calculations. For these reasons, little quantitative agreement with observations at real calenders is to be expected; cf. the results in the sections 4.4 to 4.6.

4.3 Some Remarks on the Numerical Proceeding

For a given initial state $\mathbf{u}(0) = \mathbf{u}_0$, the autonomous equation (4.1) is solved, as initial value problem, by a Matlab routine. For that purpose, at any numerically known instantaneous state $\mathbf{u}$ the function $\mathbf{f}(\mathbf{u})$ has to be computed. That is trivial for $\mathbf{f}_2$, cf. $(4.2)_2$, and, as outlined in Sect. 2.3, fairly easy and efficiently done for most of the terms of $\mathbf{f}_1$, cf. $(4.2)_1$, except $\mathbf{f}_c$ which represents the integrals of (3.34). These integrals have to be evaluated along $s_1 \le s \le s_2$, the region of the nip at the instant. First, the values of s_1, s_2 follow, after appropriate numerical combinations of the relevant equations of Sect. 3, by approximate numerical solutions of (3.14) and (3.15), respectively. Yet, in (3.15), the extreme value ε_m – necessary to determine the residual stress σ_r and the strain ε_r from (3.16), (3.17) – is taken at $s = s_m$, obtained numerically from the condition $\partial\varepsilon_p/\partial s = 0$, where instantly the compression (the loading) interval of the paper ends and the resilience (the unloading) begins. With s_1, s_m, ε_r, s_2 known, secondly, the integrals for the loading and the unloading interval (length about 5 mm, and 3 mm, respectively) are computed by the trapezoidal rule (each with three subsections of equal length), the integrands being calculated numerically at the support points by the relevant formulas of that section.

4.4 Stationary Operation

At stationary motion, subscripts $..._S$, the machine runs without oscillating at constant angular velocities $\Omega_1 = \Omega_N$, Ω_{2S}, cf. (2.4), (2.7), and constant paper velocity $v_P = v_{PS}$, cf. $(2.8)_2$. The stationary state $\mathbf{u} = \mathbf{u}_S$ follows from the right-hand side of (4.1), which is established numerically, cf. Sect. 4.3, and solved by Newton's method:

$$\mathbf{f}(\mathbf{u}_S) = \mathbf{0}. \tag{4.3}$$

Table 1 lists the non-vanishing elements of $\mathbf{u}_S$ resulting for the parameters of Appendix A.4:

Table 1: Stationary displacements, angular velocities, paper velocity

$\Omega_{1S} = \Omega_N = 11.500$ Hz		$x_{1S} = -2.671$ µm		$y_{1S} = 1325.5$ µm			
$q_{3...9S}$, µm	111.2	-54.94	709.5	6.918	122.8	0.931	32.264
$q_{10...16S}$, µm	-0.00431	-0.00860	0.00117	0.06708	1.340	0.05248	2.103
$q_{17...23S}$, µm	0.3959	-709.4	-54.90	-245.66	13.86	-96.80	2.807
$\Omega_{2S} = 8.187$ Hz		$x_{2S} = 1.304$ µm		$y_{2S} = -227.61$ µm		$v_{PS} = 25.00$ m/s	
$q_{27...33S}$, µm	-0.00196	0.01025	1.507	0.00518	1.521	0.00346	0.9419
$q_{34...40S}$, µm	0.000561	0.00112	-0.00409	0.00127	0.05776	0.00176	0.2070
$q_{41...47S}$, µm	34.889	-2.0123	0.00813	-3.181	0.00884	-2.884	-0.00928

The upper half of Table 1 holds for roll 1, the lower half for roll 2; the displacements $\mathbf{q}_S$ are arranged corresponding to the rows of equations (2.3), (2.4).

Since the parameters are surmised only roughly it is not possible to compare the results to the state of a real machine quantitatively. But it is obvious that the deformations of the thick-walled upper roll could have been neglected. Likewise, the shear deformations (cf. Table 1, lines 3 and 7) might have been neglected for both are small compared to the other deformations.

Maybe some details of the proceedings in the nip are of interest because they would be difficult to watch or measure on a machine, cf. Figure 7. The nip has the length $l = s_1 - s_2 = 8.92$ mm. Figure 7a shows the paper impression $h(s)$. Its maximum, near $s = 0$, amounts to about 0.075 mm. At the exit s_2 remains a compression of about 0.05 mm. Whilst the upper part of the impression $h(s)$ lies nearly symmetrically with respect to $s = 0$, the

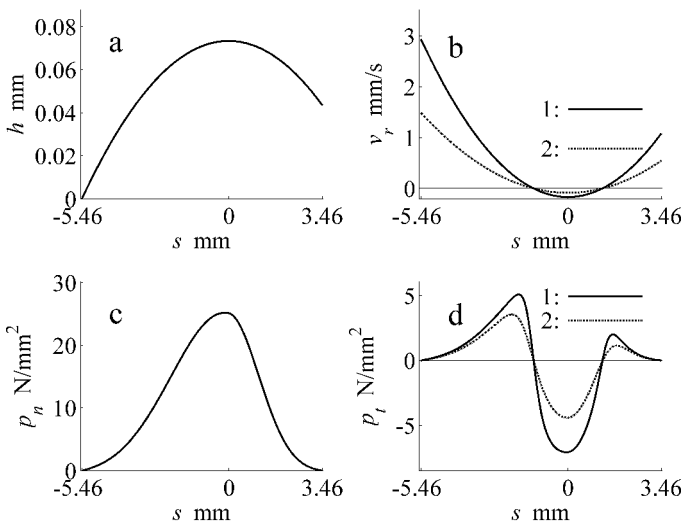

Figure 7: Proceedings in the nip. a) Paper impression, b) relative velocities between paper and rolls 1,2, c) normal pressure, d) tangential stresses between paper and rolls 1,2

curve of the normal pressure $p_n(s)$ is oblique, see Figure 7c. That is due to the hysteretic stress strain relation, cf. Figure 4, and to the damping, cf. (3.18). Figure 7b presents the relative velocities between the paper and the rolls 1, 2. Both change their signs twice along the nip at nearly – not exactly – the same place s. Note that the corner velocities $v_c = \pm$ 0.1 mm/s, see Figure 6 and Table A.7, lie close to the minimum relative velocities. This means that the friction need not reach its Coulomb values $\pm\mu_0$. The normal pressure assumes its maximum in that neighborhood, cf. Figure 7c, the tangential stresses reach their (absolute) maximal values in the region of negative relative velocities (see Sect. 3.4 for the orientations). The tangential stresses keep equilibrium with the forces F1, F2, cf. Figure 1.

4.5 Variational Equation and Stability

Small variational oscillations $\delta\mathbf{u} = \mathbf{v}(t)$ about the stationary state $\mathbf{u}_S(t)$ of Sect. 4.4, i.e. motions

$$\mathbf{u}(t) = \mathbf{u}_S + \delta\mathbf{u} = \mathbf{u}_S + \mathbf{v}(t), \tag{4.4}$$

are governed by the autonomous variational equation

$$\dot{\mathbf{v}} = \mathbf{A}\,\mathbf{v}, \tag{4.5}$$

where $\mathbf{A}$ is the Jacobian (matrix) of the derivative of $\mathbf{f}(\mathbf{u})$ at $\mathbf{u}_S$ (cf. Bullo et al. 2005):

$$\mathbf{A} = \mathbf{D}\,\mathbf{f}(\mathbf{u}_S), \tag{4.6}$$

which is calculated numerically from $\mathbf{f}(\mathbf{u})$, the right-hand side of (4.1).

For the normal oscillations $\mathbf{v} = \hat{\mathbf{v}}\exp(\lambda t)$ about the stationary motion follows from (4.5) the eigenvalue problem

$$\lambda\,\hat{\mathbf{v}} = \mathbf{A}\,\hat{\mathbf{v}}. \tag{4.7}$$

The eigenvalues λ_k, i.e. the (complex) roots of the characteristic equation to (4.7), are written in two forms:

$$\lambda_k = \delta_k + \mathrm{j}\omega_k,\ \ \tilde{\lambda}_k := \lambda_k/(2\pi) =: \tilde{\delta}_k + f_k\ \mathrm{j}, \tag{4.8}$$

so that the natural frequencies f_k are measured in Hertz (Hz).

4.5.1 Numerical Values of the Normal Oscillations about the Stationary State $\mathbf{u}_S$ of Section 4.4

Table 2 shows the two large negative eigenvalues $\tilde{\lambda}_1, \tilde{\lambda}_2$ and the 46 complex eigenvalues $\tilde{\lambda}_{3\ldots48}$, with positive imaginary parts, ordered by descending magnitude. Not shown are two vanishing eigenvalues and the complex conjugates to the $\tilde{\lambda}_k$.

Table 2: Eigenvalues $\tilde{\lambda}_k = \tilde{\delta}_k + f_k$ j Hz (i.e.: real and imaginary parts of λ are divided by 2π)

$\tilde{\lambda}_{1...4}$	-2.0378 ·10^8	-3.3400 ·10^5	-0.34563 + 12931 j	-0.009219 + 12847 j
$\tilde{\lambda}_{5...8}$	-0.16766 + 12747 j	-0.007982 + 12688 j	-0.04398 + 12636 j	-0.001271 + 12609 j
$\tilde{\lambda}_{9...12}$	-45.685 + 10262 j	-1.2571 + 8513.8 j	-1.3881 + 8423.4 j	-0.67349 + 8273.0 j
$\tilde{\lambda}_{13...16}$	-0.67851 + 8201.8 j	-0.28294 + 8124.4 j	-0.21616 + 8088.4 j	-62.668 + 6435.4 j
$\tilde{\lambda}_{17...20}$	-0.8544 + 3778.1 j	-4.3301 + 3519.3 j	-4.8957 + 3226.8 j	-5.7824 + 3058.1 j
$\tilde{\lambda}_{21...24}$	-1.5925 + 2684.2 j	-4.7444 + 2452.3 j	-6.2235 + 2323.7 j	-7.9805 + 2036.2 j
$\tilde{\lambda}_{25...28}$	-7.5313 + 1763.8 j	-7.5338 + 1616.2 j	-10.675 + 1593.4 j	-47.424 + 1476.0 j
$\tilde{\lambda}_{29...32}$	-10.942 + 1327.4 j	-6.1170 + 1246.8 j	-19.857 + 1187.2 j	-18.800 + 979.60 j
$\tilde{\lambda}_{33...36}$	-16.123 + 893.27 j	-12.588 + 878.36 j	-10.397 + 744.45 j	-10.073 + 703.59 j
$\tilde{\lambda}_{37...40}$	-9.7934 + 664.78 j	-5.3461 + 545.95 j	-0.1775 + 212.31 j	0.0024664 + 149.37 j
$\tilde{\lambda}_{41...44}$	-0.053657 + 88.456 j	-0.078737 + 83.293 j	-0.013371 + 46.693 j	-0.0060862 + 40.40 j
$\tilde{\lambda}_{45...48}$	-0.008636 + 28.673 j	-0.007034 + 24.243 j	-0.003016 + 16.522 j	-0.006305 + 7.0342 j

Some remarks: The two vanishing eigenvalues correspond to the undetermined longitudinal position of the paper and the undetermined angle of roll 2. The eigenvalue λ_1 belongs to an almost immediate brake of the paper in case it slides initially through the nip, and λ_2, likewise, holds for a sharp retard of rolls 1 and 2 slipping with respect to each other. The very high frequencies, e.g. $f_3 \approx 12\,850$ Hz, come with relatively large shear deformations of the thinner roll 1, whereas the shear deformation of the thicker roll 2 is stronger at the a bit lower frequencies, e.g. $f_{12} \approx 8\,500$ Hz. There are combinations of many terms of (2.2) to (2.8) of comparable magnitudes at, e.g., $f_{18} \approx 3\,500$ Hz. The lowest frequency, $f_{48} \approx 7$ Hz, belongs to rotational oscillations of the two rolls with respect to the flexible clutch at the drive of roll 1. (Of course, some relative rotational and translational displacements step in.) At the other lower frequencies the system oscillates mainly in its flexible suspensions, the roll bending and extensional deformations growing relatively larger and larger the higher the frequencies. (At these frequencies, again as in the stationary displacements, the deformations of the thick walled roll 2 are much smaller than those of the thin walled roll 1.)

Of special importance is the eigenvalue $\tilde{\lambda}_{40} = 0.0024664 + 149.37$ j Hz (underlined in Table 2). Since its real part is positive, meaning that $\mathbf{v}_{40}(t)$ will grow exponentially, the stationary motion $\mathbf{u}_S$ is unstable. The modal vector $\hat{\mathbf{v}}_{40}$ of that normal oscillation determines the shape of the self-excited oscillation which branches off from $\mathbf{u}_S$. (See the self-excited oscillations in Sect. 4.6.) Table 3 lists the 24 elements of $\hat{\mathbf{v}}_{40}$ which have a magnitude > 0.01. They are ordered by descending magnitude (the largest one scaled to 1), and rounded to two decimals (0.00 indicate terms < 0.01). The heavy roll 2 contributes only by small rigid body oscillations, cf. the elements k = 26, 24, 25, and the tiny deformations k = 44, 46. (So roll 2 stays almost stationary.) The center of hub 1 revolves counter-clockwise on a small ellipse (axes k = 2, 1 for y_1, x_1, respectively). The rotational oscillation, too, is small (k = 3). An oval oscillation of roll 1, combined with a translation with respect to its hub, is determined by the larger elements k = 5, 18 and the lesser ones k = 4, 19, cf. (2.3) and Figure A.1.1. Largest are the bending deformations, terms k = 22, 20, somewhat smaller 23, and 21. They certainly govern the process but details will not be discussed in this article. As above, the shear deformations, k = 16, 15, are tiny.

Table 3: The 24 largest elements of $\hat{\mathbf{v}}_{40}$

k	22	20	5	18	23	9
$\hat{v}_{40,k}$	1	-0.66 + 0.00 j	0.47 + 0.00 j	-0.47 + 0.00 j	0.00 + 0.36 j	-0.33 + 0.00 j
k	7	21	6	2	8	26
$\hat{v}_{40,k}$	0.33 + 0.00 j	0.00 + 0.29 j	0.00 + 0.15 j	0.13 + 0.00 j	0.00 + 0.12 j	-0.06 + 0.00 j
k	3	1	4	19	48	24
$\hat{v}_{40,k}$	0.00 - 0.06 j	0.00 - 0.06 j	0.00 + 0.05 j	0.00 + 0.05 j	0.00 + 0.04 j	0.00 + 0.02 j
k	16	25	15	44	46	17
$\hat{v}_{40,k}$	-0.02 + 0.00 j	0.00 + 0.01 j	0.00 + 0.01 j	0.01 + 0.00 j	0.01 + 0.00 j	0.01 + 0.00 j

4.5.2 Stabilizing and Destabilizing Parameter Changes

Stability is indispensable for stationary operation of a machine. Thus, the question arises which parameter modifications stabilize an unstable operation and which worsen the instability. Table 4 shows some effects, calculated for changes of the basic parameters of Appendix 4, upon the eigenvalue $\tilde{\lambda}_{40}$. (The real parts of the other eigenvalues $\tilde{\lambda}_k$ remain negative within the relevant regions. Inverse changes produce inverse effects.)

Table 4: Effect of parameter changes upon the critical eigenvalue $\tilde{\lambda}_{40} = 0.002466 + 149.37$ j

No.	Paramter	Modification	New $\tilde{\lambda}_{40}$ Hz	Effect
1	Suspension damping b_{x1}	+ 50 %	0.00245 + 149.37 j	tiny
2	Suspension damping b_{y1}	+ 50 %	0.00237 + 149.37 j	weak stabilization
3	Suspension damping b_{x2}	+ 50 %	0.00246 + 149.37 j	tiny
4	Suspension damping b_{y2}	+ 50 %	0.00239 + 149.37 j	weak stabilization
5	Suspension dampings $b_{S1...3}$	+ 50 %	–0.01050 + 149.37 j	strong stabilization
6	Winkler damping radial B_r	+ 50 %	0.00175 + 149.37 j	stabilizes
7	Winkler damping tangential B_{psi}	+ 50 %	0.00242 + 149.37 j	weak stabilization
8	Drive damping b_T	+ 50 %	0.00246 + 149.37 j	tiny
9	Paper damping b_p	+ 10 %	0.00261 + 149.37 j	destabilizes
10	Paper pull F_1	– 10 %	0.00387 + 149.37 j	stronger destabiliz.
11	Retarding moment of roll 2, M_r	– 10 %	0.00278 + 149.37 j	destabilizes
12	Paper stiffness E_l	+ 5 %	0.00263 + 149.37 j	destabilizes
13	Paper stiffness E_{ul}	+ 5 %	0.00236 + 149.37 j	stabilizes
14	Paper thickness	+ 5 %	0.00248 + 234.58 j	weak destabilizat.
15	Corner velocity v_{c1}	+ 50 %	0.00430 + 149.37 j	stronger destabiliz.
16	Corner velocity v_{c2}	+ 50 %	0.00193 + 149.37 j	stabilizes
17	Coulomb friction μ_{01}	+ 5 %	0.00289 + 149.37 j	destabilizes
18	Coulomb friction μ_{02}	+ 5 %	0.00253 + 149.37 j	destabilizes
19	Suspension roll 1, angle α_2	+ 5 %	0.00038 + 149.72 j	stronger stabilizat.
20	Suspension roll 1, angle α_3 ($\times$ 1.05)	+ 5 %	0.00368 + 149.72 j	stronger destabiliz.

An increase of the hub dampings b_x, b_y has little stabilizing effect, see lines 1 to 4, since there are small displacements only, cf. Table 3. Because of the large local motions at the three-point suspension, see Figure A.1.2 and Table 3, an increase of the b_S stabilizes drastically. At first glance several of the other results are surprising, for example the strong influence of the pull at the paper, line 10, or the effects of the frictions between paper and rolls acting inversely to each other (because of their opposing orientations), cf. the lines 15 to 18. A change of the angles at the three-point suspension, again, has large effects, see lines 19 and 20. Thus, concluded from this model, that suspension is the most promising place for stabilizing manipulation. (It seems to be the only place to exert an external moment locally upon the wall of roll 1.)

4.6 Self-excited Oscillations

It is not easy to find an appropriate initial state $\mathbf{u}_0$, cf. Sect. 4.3, to start a run up of the calender without bumping of the rolls (temporary auxiliary dampings are helpful). Thereafter – because of the many small real parts of the eigenvalues in Table 2 – it takes a period of about 5 minutes (machine time) till the transients vanish. (Since there are several weakly damped normal modes of high frequencies, cf. Table 2, the numerical integration is slow.) Figure 8 shows a sketch of the phase curves of the 46 roller states in normalized form. Even the oscillations of the shear deformations, k = 10,...,16, and k = 34,...,40 (having tiny amplitudes, cf. Table 5) are periodic. (See below, for the deviations at k = 1, 3, 4, 19.) Therefore, a numerical Fourier transform is possible,

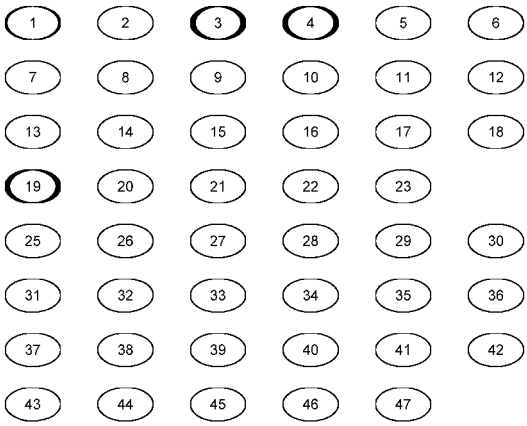

Figure 8: Phase curves $\dot{q}_k$ over q_k, k = 1,...,23 and k = 25,...,47; normalized (amplitudes in Table 5)

$$\mathbf{u}(t) = \mathbf{U}_0 + \mathrm{Re}\sum_{n'} \mathbf{U}_{n'} \exp\left(2\pi\ \mathrm{j}\, f_{n'} \cdot t\right), \tag{4.9}$$

where the $\mathbf{U}_{n'}$, and $f_{n'}$ are relevant complex amplitudes and frequencies (subscripted by n'), respectively.

The vectors $\mathbf{U}_0$ and $\mathbf{u}_S$, cf. Table 1, agree up to two, three digits. The dominating non-constant Fourier term oscillates with the frequency $f_{1'} \approx 150$ Hz which is very close to f_{40} = 149.37 Hz, see Table 2. Table 5 lists the complex amplitudes $\mathbf{U}_{1'}$ rounded to two decimals. They indicate the dimensions of the phase curves in Figure 8. Again, the $\mathbf{U}_{1'}$ are closely related to $\hat{\mathbf{v}}_{40}$.

Table 5: Complex amplitudes $U_{1',k}$ of the dominating Fourier term (150 Hz) of the self-excitation

$U_{1',1...6}$ µm	0.01-2.08j	4.68+0.01j	-0.03-2.08j	-0.03+1.98j	17.05-0.01j	0.02+5.22j
$U_{1',7...12}$ µm	11.95-0.02j	-0.02+4.34j	-11.98+0.00j	0.00+0.01j	0.00+0.01j	0.00+0.00j
$U_{1',13...18}$ µm	0.00+0.07j	0.13+0.00j	-0.00+0.29j	-0.77+0.00j	0.20+0.00j	-16.86+0.00j
$U_{1',19...24}$ µm	-0.03+1.91j	-23.80+0.03j	0.04+10.37j	35.89+0.00j	-0.06+12.98j	–
$U_{1',25...30}$ µm	0.00+0.51j	-2.31+0.01j	0.00-0.01j	0.00-0.03j	-0.03+0.00j	0.00-0.02j
$U_{1',31...36}$ µm	-0.13+0.00j	0.00-0.00j	-0.08+0.00j	0.00-0.01j	0.00-0.01j	0.00+.0.00j
$U_{1',37...42}$ µm	0.00-0.00j	-0.01+0.00j	0.00-0.010j	-0.02+0.00j	0.05+0.00j	0.09-0.00j
$U_{1',43...48}$ µm	0.00-0.01j	0.28-0.00j	-0.00-0.01j	0.25-0.00j	-0.00+0.01j	–

If $\hat{\mathbf{v}}_{40}$ is scaled to equal phase and amplitude with respect to the element k = 22 of $\mathbf{U}_{1'}$, the numbers of the vectors agree up to three digits; compare the relative magnitudes of Table 3 and the ratios of the magnitudes of the corresponding terms in Table 5.

The second largest Fourier term oscillates with $f_{2'} \approx 17$ Hz. It corresponds to the normal oscillation $\mathbf{v}_{47}$ with f_{47} = 16.52 Hz, cf. Table 2. Appreciable magnitudes occur only in the displacements k = 3, 4, 19, 1, 21 (descending order, the largest ≈ 7% of the 150 Hz oscillation), see Figure 8. Again, the values are closely related to the normal mode calculated. Furthermore, there are, in some of the displacements only, barely perceptible oscillations with frequencies $2{\cdot}f_{2'}$, and $2{\cdot}f_{1'}$ as well as $3{\cdot}f_{1'}$.

Of course, the one dominating Fourier term, the smooth appearance of the phase curves in Figure 8, means that the self-excited oscillation proceeds very regularly, almost without noise, i.e. Fourier terms with frequencies (far) above the self-excitation. Maybe, the interaction of the rolls at the nip is too local to produce coupled oscillations with diverse Fourier terms of comparable sizes.

In the vibrating system, the proceedings in the nip look similar as shown in Figure 7, except that the quantities oscillate slightly about their stationary values. Figure 9a shows the oscillations of the relative velocities v_{rel1}, and v_{rel2} between the paper and rolls 1 and 2, respectively, at s = -3 mm, about halfway between the left border of the nip and the point of maximum impression, cf. Figure 7b.

Due to the high normal pressure, see Figure 7c, and the large friction coefficients, $\mu_{01} = 0.30$, $\mu_{02} = 0.25$, there is little macro slip between paper and rolls. Roll 1 and paper oscillate, relatively, in counter phase, roll 2 and paper in phase. The magnitudes of the slip lie in the range of $0.5 \cdot 10^{-4}$ to $1.5 \cdot 10^{-4}$, cf. Figure 7b, (nominal paper speed v = 25 m/s).

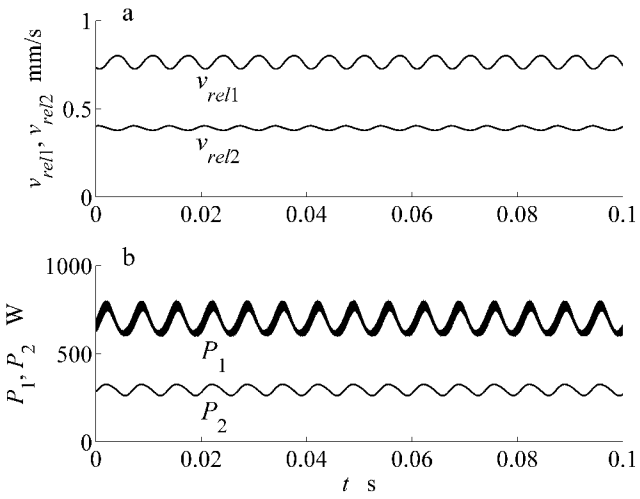

Figure 9: Self-excited oscillations. a) Relative velocities v_{rel1}, v_{rel2} between rolls and paper at s = -3 mm, b) frictional power P_1, P_2 between rolls and paper

A simple model for abrasive wear bases on the assumption that abrasion is proportional to the frictional power, defined as product of relative velocity and tangential (i.e. frictional) contact force; see (Fleischer et al. 1980) for details. With v_{rel} from (3.27) and p_t from (3.30) follows, cf. (3.34),

$$P(t) = \int_{s_1(t)}^{s_2(t)} p_t(s,t)\, v_{rel}(s,t)\, \mathrm{d}s . \qquad (4.10)$$

Figure 9b shows $P_1(t)$ and $P_2(t)$ for the rolls 1 and 2, respectively, for the machine of the width b = 1 m. The average values are 700 W and 290 W, the widths of the fluctuations 200 W and 60 W, respectively. Of course, the fluctuations oscillate with $f_{1'}$ = 150 Hz. A numerical Fourier analysis discloses that both, P_1 and P_2, contain components oscillating with $2 \cdot f_{1'}$, – because of the product in the integrand of (4.10).

5 Summary, Conclusions, Outlook

The rolls are assumed to deform like thick elastic rings in the case of plane strain. In the circumferential direction they undergo extension, bending by the Bernoulli-Euler hypothesis (like a curved beam), and shear deformation according to Timoshenko's hypothesis. Appendix A.1 develops the details, adds suspensions and drive, introduces dampings. Appendix A.2 lists the linear – the machine dynamic – terms of the dicretized equations of motion of Sections 2.2, 2.3. The nonlinear geometric, kinematical and dynamical relations in the contact zone between paper and rolls, the nip, are established in Sect. 3; the corresponding coefficients for the numerical calculation are listed in Appendix A.3. For the somewhat arbitrarily selected parameters of Appendix A.4, Sect. 4 presents numerical solutions to the problem.

The calender oscillates self-excited at about 150 Hz nearly sinusoidal about (an unstable) stationary state. The shape of this oscillation corresponds closely to the characteristic mode $(\tilde{\lambda}_{40}, \hat{\mathbf{v}}_{40})$ of the variational equation about that stationary state, cf. Sect. 4.5.1 and Sect. 4.6. Counting the natural frequencies, as customary, from below, this is the 9th critical speed, see Table 2. (The frequencies of revolution of both rolls lie between the first and the second critical speeds, cf. Table 1 and Table 2.) The oscillations are sustained by energy exchange in the nip. It can be envisioned a bit by interpreting the larger elements of $\hat{\mathbf{v}}_{40}$, listed in Table 3, and the effects of parameter-changes on the exponential growth of that mode, shown in Table 4.

The oscillatory 3rd and 2nd order wall-bending, some ring displacements (mainly with respect to the hub which remains almost stationary), and 3rd order wall-extensions at the lower, lighter, driven roll 1 (radius R_1 = 310 mm, wall thickness $2 \cdot a_1$= 72 mm) determine the shape variations of the nip and the kinematics there, cf. Table 3 together with equation (2.3). The stronger these motions interact with the parameter changes of Table 4 – intuitively conceivable as virtual work – the larger are the effects of the changes upon the behavior of the system. Obviously, the closer – in the literal sense – these changes are placed to the nip, the more efficiently they alter the behavior. Thus, it is easy to stabilize the system by an increase of the damping in the three-point suspension, cf. Table 4, line 5, and Figure A.1.2.

The model has several deficiencies. Table 4 shows that viscous terms in and near the nip have large influence on the stability of the steady operation. Therefore, it will be essential to incorporate the visco-elastic cover of the

lower roll into the model. Furthermore, as in (Brommundt, 2007) the highest order bending modes taken into account – there the 2nd , here the 3rd – govern the process. Thus, further higher order bending modes should be taken into account. Which mechanism limits that order? Some material damping might be the answer. (That will accelerate the numerical integration, too.) Certainly, the paper is not only vertically compressible but also sheared transversely and strained longitudinally. Equally important is a careful model of the roll's supports. The support of the lower roll will certainly be anisotropic, thus – in combination with the higher order bending modes – might effect drastically the stability.

On the rotating rolls, the periodic change of the friction power (cf. P_1, P_2 in Figure 9b) – frequencies transformed to the rolls – will grind periodic wave patterns into their surfaces. The synchronization necessary for that process could be provided by omnipresent small deviations of the rolls from circularity (some μm are sufficient) which enter the model threefold: disturb the nip kinematics, produce angle ψ-dependent stiffness, lead to unbalance forces. The newly ground waves will establish a regenerative wear mechanism collaborating with the initial one.

A numerical simulation of such process should start from an improved model as outlined in the paragraph above. The synchronization can be calculated in a way similar to Brommundt (2004); various interactions between the rolls (see Kovriguine et al. I, II, 1998) are to be expected. The ensuing regenerative wear is closely related to the polygonalization of railway wheels and could be studied correspondingly, cf. Brommundt (1996). Likely, the required amount of work is too high for many engineers. For them it might be an alternative to restrict their study to an improved model with circular rolls along the ways of this paper. That will provide parameter sensitivities, cf. Table 4, which, after some experimental tests, may become sufficient to improve the operational stability of calenders: To suppress the triggering effect may be helpful already.

Appendix A.1: Basic Equations of the System

We establish the basic relations for the displacements, deformations and kinematical conditions at the rolls as well as the potential, the kinetic energy and the damping terms..

A.1.1 Displacements

Following the remarks in Sect. 2.1 we discuss the deformation of ring 1 in a general way, dropping the subscripts. Figure A.1.1a shows the Cartesian basis $(\vec{e}_x,\vec{e}_y,\vec{e}_z)$, $\vec{e}_z=\vec{e}_x\times\vec{e}_y$, and the cylinder basis $(\vec{e}_\psi,\vec{e}_r,\vec{e}_z)$, $\vec{e}_z=\vec{e}_\psi\times\vec{e}_r$, in a form convenient for our purpose. There hold

$$\begin{aligned}\vec{e}_\psi &= \vec{e}_x\cos\psi - \vec{e}_y\sin\psi,\ \vec{e}_r = \ \vec{e}_x\sin\psi + \vec{e}_y\cos\psi,\\ \vec{e}_x &= \vec{e}_\psi\cos\psi + \vec{e}_r\sin\psi,\ \vec{e}_y = -\vec{e}_\psi\sin\psi + \vec{e}_r\cos\psi.\end{aligned} \tag{A.1.1}$$

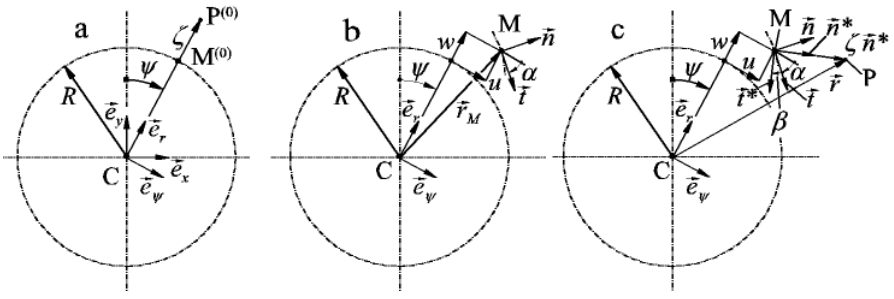

Figure A.1.1: Deformations of the lower ring. a) initial shape, b) bending and azimuthal displacements at the midline, c) displacements by bending and shear deformation; (all drawn disproportionately)

Let, for the time being, the center C of the ring be fixed to $(x,y) = (0,0)$. Initially, with respect to C, a point $M^{(0)}$ of the midline, polar coordinates (ψ,R) and a material point $P^{(0)}$ of the ring, polar coordinates $(\psi,R+\zeta)$, have the positions

$$\vec{r}_M^{(0)} = R\,\vec{e}_r(\psi),\ \ \vec{r}^{(0)} = (R+\zeta)\,\vec{e}_r(\psi), \tag{A.1.2}$$

respectively, see Figure A.1.1a. The system of the material coordinates, $(\psi,R+\zeta)$, $-\pi \le \psi \le \pi$, $-a \le \zeta \le a$, is orthogonal. The extensional and the bending deformations of the ring are measured at the midline by the displacements $u = u(\psi,t)$, $w = w(\psi,t)$, see Figure A.1.1b. They move the midline point to M:

$$\vec{r}_M = (R+w)\,\vec{e}_r + u\,\vec{e}_\psi\,. \tag{A.1.3}$$

Differentiation of (A.1.3) with respect to ψ, with $(\cdot)' = \partial(\cdot)/\partial\psi$ and

$$U := u - w',\ W := w + u',\ \tan\alpha := \frac{U}{R+W}, \tag{A.1.4}$$

leads to the tangent vector $\vec{t}$ and the normal vector $\vec{n}$, outwards positive, see Figure A.1.1b, such that

$$\vec{t} = \frac{-U\,\vec{e}_r + (R+W)\,\vec{e}_\psi}{\sqrt{(R+W)^2+U^2}},\ \vec{n} = \frac{(R+W)\,\vec{e}_r + U\,\vec{e}_\psi}{\sqrt{(R+W)^2+U^2}},\ \begin{pmatrix}\vec{t}\\ \vec{n}\end{pmatrix} = \begin{pmatrix}\cos\alpha & -\sin\alpha\\ \sin\alpha & \cos\alpha\end{pmatrix}\begin{pmatrix}\vec{e}_\psi\\ \vec{e}_r\end{pmatrix}. \tag{A.1.5}$$

To care for the shear deformation of the ring, the shear angle $\beta = \beta(\psi,t)$ is added to the rotation by the angle α in $(A.1.5)_3$, cf. $(A.1.4)_3$ and Figure A1.1c. This leads to

$$\begin{pmatrix}\vec{t}^{\,*}\\ \vec{n}^{\,*}\end{pmatrix} = \begin{pmatrix}\cos\beta & -\sin\beta\\ \sin\beta & \cos\beta\end{pmatrix}\begin{pmatrix}\vec{t}\\ \vec{n}\end{pmatrix} = \begin{pmatrix}\cos(\alpha+\beta) & -\sin(\alpha+\beta)\\ \sin(\alpha+\beta) & \cos(\alpha+\beta)\end{pmatrix}\begin{pmatrix}\vec{e}_\psi\\ \vec{e}_r\end{pmatrix}. \tag{A.1.6}$$

The shear angle β is the third displacement of the ring. (To get the dimension length for all three displacements, we express β by $v = v(\psi,t) := R\cdot\beta(\psi,t)$.) Corresponding to the Bernoulli-Euler hypothesis and with Timoshenko's assumption the resulting position of the point P, shown in Figure A1.1c, is given by:

$$\begin{aligned}\vec{r} = \vec{r}(\psi,\zeta,t) &= (R+w)\,\vec{e}_r + u\,\vec{e}_\psi + \zeta\,\vec{n}^{\,*}\\ &= \big(R+w+\zeta\cos(\alpha+\beta)\big)\,\vec{e}_r + \big(u+\zeta\sin(\alpha+\beta)\big)\,\vec{e}_\psi\,.\end{aligned} \tag{A.1.7}$$

Expansion up to the second order of (u,v,w) leads to

$$\vec{r} = \Big(R+w+\zeta\,\big(1-(U+v)^2/2R^2\big)\Big)\,\vec{e}_r + \Big(u+\zeta\,\big((U+v)/R - UW/R^2\big)\Big)\,\vec{e}_\psi\,. \tag{A.1.8}$$

The mean material angular rotation produced by the displacement $\vec{r}$, measured along the midline, cf. Figures A.1.1b and A.1.3, is given by the average:

$$\Phi_m = \frac{1}{2\pi}\int_{\psi=-\pi}^{\pi} \operatorname{atan}\left(\frac{u}{R+w}\right)\mathrm{d}\psi \approx \frac{1}{2\pi}\int_{\psi=-\pi}^{\pi}\frac{u}{R}\left(1-\frac{w}{R}\right)\mathrm{d}\psi \approx \frac{1}{2\pi}\int_{\psi=-\pi}^{\pi}\frac{u}{R}\,\mathrm{d}\psi; \tag{A.1.9}$$

i.e. in general form, up to the second and the first order, respectively.

A.1.2 The Potential

Hamilton's principle requires the potential. There are three contributions: The potentials of the elastic deformation of the rolls, the potentials of the elastic suspensions of the rolls, and the potentials of the weights.

We follow Washizu 1982, Chapters 3, 4, to formulate the potential of the elastic deformation. For formal reasons, for plane strain, temporarily, $\vec{r}^{\,(0)} + z\,\vec{e}_z \Rightarrow \vec{r}^{\,(0)}$ and $\vec{r} + z\,\vec{e}_z \Rightarrow \vec{r}$ are introduced. Let $(\alpha^1,\alpha^2,\alpha^3) := (\psi,\zeta,z)$. Then hold the covariant base vectors

$$\vec{g}_j = \frac{\partial\vec{r}^{\,(0)}}{\partial\alpha^j},\ \vec{G}_j = \frac{\partial\vec{r}}{\partial\alpha^j},\ j = 1,2,3, \tag{A.1.10}$$

the (elements of the) covariant metric tensors g_{jk}, G_{jk} as well as the strains f_{jk} with respect to (ψ,ζ,z):

$$g_{jk} = \vec{g}_j \cdot \vec{g}_k,\ G_{jk} = \vec{G}_j \cdot \vec{G}_k,\ f_{jk} = (G_{jk} - g_{jk})/2,\ j,k = 1,2,3. \tag{A.1.11}$$

After scaling corresponding to $((R+\zeta)\cdot\psi,\zeta,z)$ follow the two non-vanishing normalized strains

$$\begin{aligned} e_{11} = \frac{1}{2(R+\zeta)^2}\Big[& U^2 + 2RW + W^2 + \zeta^2(2+\alpha'+\beta')(\alpha'+\beta') \\ & + 2\zeta\,(1+\alpha'+\beta')\big(U\sin(\alpha+\beta) + W\cos(\alpha+\beta)\big) \\ & + 2\zeta R\,\big((1+\alpha'+\beta')\cos(\alpha+\beta) - 1\big)\Big], \\ e_{12} = \frac{1}{2(R+\zeta)}\ & \big[(R+W)\sin(\alpha+\beta) - U\cos(\alpha+\beta)\big]. \end{aligned} \tag{A.1.12}$$

For isotropic material we get the strain energy function

$$A = \frac{E}{2}\frac{1-\nu}{(1+\nu)(1-2\nu)}\,e_{11}^2 + 2G\,e_{12}^2, \text{ abbreviated: } A = \frac{E_1}{2}\,e_{11}^2 + 2G\,e_{12}^2, \tag{A.1.13}$$

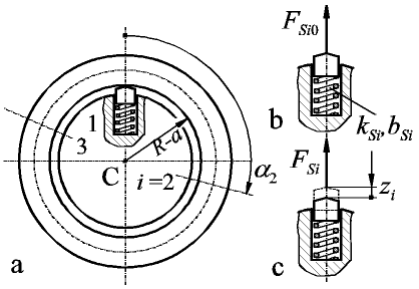

Figure A.1.2: a) Three-point suspension, in centered nominal position with b) preload F_{Si0}, c) positive load F_{Si}, and displacement z_i with respect to nominal position

where E – Young's modulus, ν – Poisson's ratio, $G = E/2(1+\nu)$ – shear modulus. As mentioned in Sect. 2.1, for better intuition, instead of a plane model, let us assume the rolls to have the length b = 1 m. Then follows the elastic potential by integrating A over the roll's volume:

$$U_R = \int_{\psi=-\pi}^{\pi}\int_{\zeta=-a}^{a} (R+\zeta)\,b\,A\,\mathrm{d}\zeta\,\mathrm{d}\psi. \tag{A.1.14}$$

To retain linear terms of the variables u, v, w and their derivatives with respect to ψ in the equations of motion, second order terms must be kept in U_R. After some manipulation we get from the preceding formulae

$$U_R = \frac{1}{2}\int_{\psi=-\pi}^{\pi}\left\{\frac{E_1 I_R}{R^3}(v'-w-w'')^2 + \frac{E_1 A_R}{R}(u'+w)^2 + \frac{GA_S}{R}v^2\right\}\mathrm{d}\psi, \tag{A.1.15}$$

where E_1I_R, E_1A_R, GA_S are the bending, the azimuthal and the shear stiffness, respectively:

$$E_1 I_R := bR^3 E_1\left[\ln\left(\frac{R+a}{R-a}\right) - \frac{2a}{R}\right],\ E_1 A_R := 2abE_1,\ GA_S := bRG\ln\left(\frac{R+a}{R-a}\right). \tag{A.1.16}$$

In the real machine, the lower roll is mounted on hydrostatic bearings, see, e.g., Figure 3.8 in van Haag (1993). We approximate that support by three suitably placed spring-dashpot elements, as sketched in Figure A.1.2: There the spring-dashpot elements i = 1, 2, 3, stiffness k_{Si}, damping b_{Si}, preload F_{Si0} (compression negative), are arranged radially (dashpots not shown). The body of this assembly (the hub) is suspended and displaced at its center C_1 as shown in Figure 1 but does not rotate. The total potential of the forces reads

$$U_{H1} = \sum_{i=1}^{3}\left(F_{Si}z_i + \frac{1}{2}k_{Si}z_i^2\right) + \frac{1}{2}\left(k_{x1}(x_1 - a_{x1})^2 + k_{y1}(y_1 - a_{y1})^2\right). \tag{A.1.17}$$

The hub of the upper roll, again suspended and displaced at its center C_2 as shown in Figure 1, is assumed to be attached to the roll by an elastic Winkler foundation acting upon the roll along its midline, cf. Figure A.1.1b, (distributed) stiffnesses K_ψ in the azimuthal direction, and K_r radially. From (A.1.8) follow, for $\zeta = 0$, linear, the displacements u, w respectively. Then holds the potential

$$U_{H2} = \frac{1}{2}\Big(k_{x2}\,(x_2 - a_{x2})^2 + k_{y2}\,(y_2 - a_{y2})^2\Big) + \frac{1}{2}\int_{\psi=-\pi}^{\pi} R\Big(K_\psi\,u^2 + K_r\,w^2\Big)\,\mathrm{d}\psi. \tag{A.1.18}$$

Let the flexible drive from the motor, torsional stiffness k_T, act on the material midline of the lower roll, see angle Φ_m in (A.1.9). With a shift angle φ_{N0} of the clutch follows the drive potential

$$U_D = \frac{1}{2}k_T\,(\Phi_m - \varphi_{N0})^2. \tag{A.1.19}$$

To establish the potential of the weight, the position vector $\vec{r}_{0P}$ from the origin 0 of the (inertial) coordinate system (0,*x,y*) to the point P of the deformed ring is required, cf. Figures 1 and A.1.1c:

$$\vec{r}_{0P} = x(t)\,\vec{e}_x + y(t)\,\vec{e}_y + \vec{r}(\psi,\zeta,t). \tag{A.1.20}$$

Then the weight potential U_W follows with the density ρ and the gravity acceleration g, pointing in the direction of $\mp\vec{e}_y$ at the lower and the upper roll, respectively:

$$U_W = \pm m_H\,g\,y \pm \int_{\psi=-\pi}^{\pi}\int_{\zeta=-a}^{a} (R+\zeta)\,b\,\rho\,g\,(\vec{e}_y\cdot\vec{r}_{0P})\,\mathrm{d}\zeta\,\mathrm{d}\psi, \tag{A.1.21}$$

where the first term on the right side is the contribution of the hub of the mass m_H.

A.1.3 Kinematics and Kinetic Energy

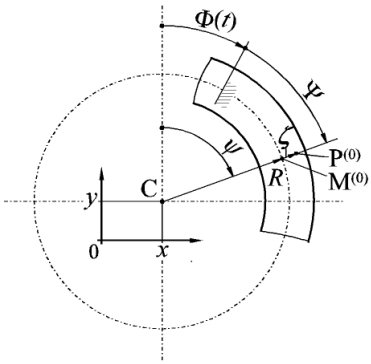

Figure A.1.3: Kinematical relations

The locations of the contact boundaries are formulated most suitably with respect to Eulerian coordinates, the (material) relative velocities require a Lagrangian view. Thus, in Figure A.1.3 we have to alternate between the angles ψ and Ψ. The Figure shows the undeformed (lower) ring at the time *t*. The position of its center C is given by the coordinates ($x(t)$,$y(t)$). From an initial position it is rotated by the angle $\Phi(t)$. With respect to the rotating frame, the material point P has the (Lagrangian) coordinates (Ψ,ζ), cf. Figure A1.1a and Figure A1.3. The position vector $\vec{r}_{0P}$, cf. (A.1.20), gets then the form

$$\vec{r}_{0P} = x(t)\,\vec{e}_x + y(t)\,\vec{e}_y + \vec{r}\,\big(\Phi(t)+\Psi,\zeta,t\big), \tag{A.1.22}$$

where ($\Phi(t)$+Ψ) replaces the argument ψ in the terms on the right hand side of (A.1.7), (A.1.8). This is the Lagrangian description of the motion.

The (material) time derivative of $\vec{r}_{0P}$ is given by

$$\vec{r}^{\,\circ}_{0P} = \frac{\mathrm{D}\vec{r}_{0P}}{\mathrm{D}t} = \dot{x}\,\vec{e}_x + \dot{y}\,\vec{e}_y + \dot{\Phi}\,\vec{r}\,' + \dot{\vec{r}}; \tag{A.1.23}$$

here are $\vec{r}\,', \dot{\vec{r}}$ the partial derivatives of $\vec{r}(\psi,\zeta,t)$ with respect to ψ and *t*, respectively. The result is the velocity $\vec{v}^{\,*}_P = \vec{v}^{\,*}_P(\Psi,\zeta,t) = \vec{r}^{\,\circ}_{0P}$ in Lagrangian notation. (Higher order time derivatives are obtained correspondingly.)

For the Euler view, after the differentiation (A.1.23) one has to step back to ($\Phi(t)$+Ψ) => ψ and gets $\vec{v}_P = \vec{v}_P(\psi,\zeta,t)$:

$$\vec{v}_P = \dot{x}(t)\,\vec{e}_x + \dot{y}(t)\,\vec{e}_y + \dot{\Phi}(t)\;\vec{r}\,'(\psi,\zeta,t) + \dot{\vec{r}}\,(\psi,\zeta,t). \tag{A.1.24}$$

The kinetic energy of the roll is given by

$$T_R = \frac{1}{2} \int_{\psi=-\pi}^{\pi} \int_{\zeta=-a}^{a} (R+\zeta)\, b\, \rho\, (\vec{v}_P \cdot \vec{v}_P)\, \mathrm{d}\zeta\ \mathrm{d}\psi, \tag{A.1.25}$$

where the expansion of $\vec{v}_P$, up to the second order with respect to the displacements and their time derivatives, follows from (A.1.24) by the decomposition $\vec{v}_P = \dot{x}\,\vec{e}_x + \dot{y}\,\vec{e}_y + v_r\,\vec{e}_r + v_\psi\,\vec{e}_\psi$, with

$$\begin{aligned} v_r &= \dot{w} - \Omega U + \dot{x}\sin\psi + \dot{y}\cos\psi - \frac{\zeta}{R}\Omega(U+v) + \frac{\zeta}{2R^2}\left(\Omega\left(2UW - \left((U+v)^2\right)'\right) - \left((U+v)^2\right)^{\bullet}\right), \\ v_\psi &= \dot{u} + \Omega(R+W+\zeta) + \dot{x}\cos\psi - \dot{y}\sin\psi + \frac{\zeta}{R}\left(\Omega(U+v)' + (U+v)^{\bullet}\right) \\ &\quad - \frac{\zeta}{2R^2}\left(\Omega\left(2(UW)' + (U+v)^2\right) + 2(UW)^{\bullet}\right). \end{aligned} \tag{A.1.26}$$

In the scalar product $(\vec{v}_P \cdot \vec{v}_P)$ in (A.1.25) again terms up to the second order only are retained.

The kinetic energy of the hubs reads

$$T_S = \frac{1}{2}\left(m_{H1}(\dot{x}_1^2 + \dot{y}_1^2) + m_{H2}(\dot{x}_2^2 + \dot{y}_2^2) + J_2\dot{\Phi}_2^2\right), \tag{A.1.27}$$

where the m_{Hi} denote their masses, and J_2 is the moment of inertia.

A.1.4 Virtual Displacements

By (A.1.8) and (A.1.20) follow the virtual displacements at the (material) point P, up to second order terms,

$$\begin{aligned} \delta\vec{r}_{0P} = &\quad \delta x(t)\,\vec{e}_x + \delta y(t)\,\vec{e}_y + \delta\vec{r}(\psi,\zeta,t), \text{ with} \\ \delta\vec{r} &= \left(\delta w - \zeta\,(\delta U + \delta v)(U+v)/R^2\right)\vec{e}_r + \left(\delta u + \zeta\left((\delta U + \delta v)/R - (W\delta U + U\delta W)/R^2\right)\right)\vec{e}_\psi \\ &\quad - \delta\Phi\left(U + \zeta\,(U+v)/R\right)\vec{e}_r \qquad + \delta\Phi\left(R + W + \zeta\,\left(1 + (U'+v')/R\right)\right)\vec{e}_\psi. \end{aligned} \tag{A.1.28}$$

A.1.5 Dampings

The damping effects at the non-rotating suspension points are combined in the Rayleigh function

$$R_S = \frac{1}{2}\left(b_T\dot{\Phi}_m^2 + \sum_{i=1}^{2}(b_{xi}\,\dot{x}_i^2 + b_{yi}\,\dot{y}_i^2) + \sum_{i=1}^{3} b_{Si}\,\dot{z}_i^2\right), \tag{A.1.29}$$

where the first term holds for the drive, cf. (A.1.9) and (A.1.19). With (A.1.28) and the relative parts of the velocities v_ψ, v_r, cf. (A.1.26) for $\zeta = 0$, follows the virtual work due to the damping contribution of the Winkler foundation, constants B_ψ, B_r parallel to (A.1.18):

$$\delta W_D = -\int_{\psi=-\pi}^{\pi} R\left(B_\psi\,(\dot{u} + \Omega W)\,\delta u + B_r(\dot{w} - \Omega U)\,\delta w\right)\mathrm{d}\psi; \tag{A.1.30}$$

linear terms only are taken into account.

Appendix A.2: Linear Terms of the Equations of Motion

A.2.1 The General Discrete Displacements

Here, the configuration vector $\mathbf{q} = (q_1,...,q_{24})^T$ comprises the elements $q_1 = \Phi \cdot R$, $q_2 = x$, $q_3 = y$ and the coefficients $(q_4,...,q_{24})$ of the discretizations, cf. Sect. 2.2,

$$\begin{aligned} u(\psi,t) &= q_4 + q_5\cos(\psi) + q_6\sin(\psi) + q_7\cos(2\psi) + q_8\sin(2\psi) + q_9\cos(3\psi) + q_{10}\sin(3\psi), \\ v(\psi,t) &= q_{11} + q_{12}\cos(\psi) + q_{13}\sin(\psi) + q_{14}\cos(2\psi) + q_{15}\sin(2\psi) + q_{16}\cos(3\psi) + q_{17}\sin(3\psi), \\ w(\psi,t) &= q_{18} + q_{19}\cos(\psi) + q_{20}\sin(\psi) + q_{21}\cos(2\psi) + q_{22}\sin(2\psi) + q_{23}\cos(3\psi) + q_{24}\sin(3\psi); \end{aligned} \tag{A.2.1}$$

the adaptations to the equations (2.2), (2.3), (2.4), for the lower roll, and to the equations (2.5), (2.6), (2.7), for the upper roll, follow by appropriate cancellations and/or re-numberings of elements.

A.2.2 Stiffnesses

When the discretization (A.2.1) is put into the elastic potentials (A.1.15) and (A.1.17/18/19) Lagrange's formula (2.10) becomes applicable. There result forces of the form **Kq,** where the stiffness matrix **K** is composed of several summands $\mathbf{K}_k$. Below, only the elements $k_k(i,j) \neq 0$ of the $\mathbf{K}_k$ are listed.

From (A.1.15) follow the three contributions

$$\mathbf{K}_1 = \frac{E_1 I_R}{R^3}\tilde{\mathbf{K}}_1,\ \mathbf{K}_2 = \frac{E_1 A_R}{R}\tilde{\mathbf{K}}_2,\ \mathbf{K}_3 = \frac{E_1 A_S}{R}\tilde{\mathbf{K}}_3, \tag{A.2.2}$$

where the leading coefficients are given by (A.1.16), R is the midline radius, and the elements $\tilde{k}_k(i,j)$ of the non-dimensional symmetric matrices $\tilde{\mathbf{K}}_k = \tilde{\mathbf{K}}_k^T$ are listed in Table A.1.

From (A.1.17) and (A.1.19) follow – for the lower roll – the stiffnesses $\mathbf{K}_4$, $\mathbf{K}_5$ with

$$k_4(2,2) = k_{x1},\ k_4(3,3) = k_{y1},\ k_4(4,4) = k_T / R_1^2, \tag{A.2.3}$$

and $\mathbf{K}_5$ consists of the three dyadic products, cf. Figure A.1.2,

Table A.1: Nondimensional stiffnesses $\tilde{k}_1(i,j), \tilde{k}_2(i,j), \tilde{k}_3(i,j)$ of a roll for bending, extension, shear, resp.

i,j	$\tilde{k}_1$	*i,j*	$\tilde{k}_1$	*i,j*	$\tilde{k}_1$	*i,j*	$\tilde{k}_2$	*i,j*	$\tilde{k}_2$	*i,j*	$\tilde{k}_3$
11,12	1	16,24	-24	24,24	64	7,22	-2	18,18	2	11,11	2
13,13	1	17,17	9	*i,j*	$\tilde{k}_2$	8,8	4	19,19	1	12,12	1
14,14	4	17,23	24	5,5	1	8,21	2	20,20	1	13,13	1
14,22	-6	18,18	2	5,20	-1	9,9	9	21,21	1	14,14	1
15,15	4	21,21	9	6,6	1	9,24	-3	22,22	1	15,15	1
15,21	6	22,22	9	6,19	1	10,10	9	23,23	1	16,16	1
16,16	9	23,23	64	7,7	4	10,23	3	24,24	1	17,17	1

$$\mathbf{K}_5 = \sum_{l=1}^{3} k_{Sl}\ \mathbf{d}_l\ \mathbf{d}_l^T \tag{A.2.4}$$

of the incidence vectors $\mathbf{d}_l = (d_l(1),...,d_l(24))^T$ with the non-vanishing elements

$$d_l(18)=1,\ d_l(19)=\cos\alpha_l, d_l(20)=\sin\alpha_l, d_l(21)=\cos 2\alpha_l, d_l(22)=\sin 2\alpha_l,\\ d_l(23)=\cos 3\alpha_l, d_l(24)=\sin 3\alpha_l. \tag{A.2.5}$$

From (A.1.18) follow – for the upper roll – the stiffnesses $\mathbf{K}_6$, $\mathbf{K}_7$, $\mathbf{K}_8$ with

$$\begin{aligned} &k_6(2,2)=k_{x2}, \qquad k_6(3,3)=k_{y2},\\ &\mathbf{K}_7 \quad =\pi R K_\psi \tilde{\mathbf{K}}_7,\ \mathbf{K}_8 \quad =\pi R K_r \tilde{\mathbf{K}}_8, \text{ where}\\ &\tilde{k}_7(4,4)=2, \tilde{k}_7(5,5)=\tilde{k}_7(6,6)=\tilde{k}_7(7,7)=\tilde{k}_7(8,8)=\tilde{k}_7(9,9)=\tilde{k}_7(10,10)=1,\\ &\tilde{k}_8(18,18)=2, \tilde{k}_8(19,19)=\tilde{k}_8(20,20)=\tilde{k}_8(21,21)=\tilde{k}_8(22,22)=\tilde{k}_8(23,23)=\tilde{k}_8(24,24)=1. \end{aligned} \tag{A.2.6}$$

A.2.3 Inertia Terms

From Sect. A.1.3, the kinetic energy, follow by dicretization and Lagrange's formula the inertia effects in the form of inertial, gyroscopic and centrifugal matrices, respectively:

$$\mathbf{M}\ddot{\mathbf{q}}+\Omega\mathbf{G}\dot{\mathbf{q}}+\Omega^2\mathbf{C}\mathbf{q}. \tag{A.2.7}$$

The matrices $\mathbf{M}=\mathbf{M}^T$, $\mathbf{C}=\mathbf{C}^T$ are symmetric, the matrices $\mathbf{G}=-\mathbf{G}^T$ are anti-symmetric.

From (A.1.25) follow, with $\tilde{a}=a/R$,

$$\mathbf{M}_1=m_R\tilde{\mathbf{M}}_1, \mathbf{M}_2=m_R\frac{\tilde{a}^2}{3}\tilde{\mathbf{M}}_2, \mathbf{G}_1=m_R\tilde{\mathbf{G}}_1, \mathbf{G}_2=m_R\frac{\tilde{a}^2}{3}\tilde{\mathbf{G}}_2, \mathbf{C}_1=m_R\tilde{\mathbf{C}}_1, \mathbf{C}_2=m_R\frac{\tilde{a}^2}{3}\tilde{\mathbf{C}}_2. \tag{A.2.8}$$

The non-vanishing elements $\tilde{m}_k(i,j), \tilde{g}_k(i,j), \tilde{c}_k(i,j)$ of the non-dimensional matrices $\tilde{\mathbf{M}}_k, \tilde{\mathbf{G}}_k, \tilde{\mathbf{C}}_k, k=1,2,$ respectively, are listed in Table A.2.

From (A.1.27) follows $\mathbf{M}_3$ with

$$m_3(1,1)=J/R^2,\ m_3(2,2)=m_3(3,3)=m_H. \tag{A.2.9}$$

A.2.4 Damping Terms

From Sect. A.1.5, dampings, follow by discretization the damping terms in the form

$$\mathbf{B}\dot{\mathbf{q}}+\Omega\mathbf{B}^r\mathbf{q}, \tag{A.2.10}$$

where the (ordinary) damping matrices $\mathbf{B}=\mathbf{B}^T$ are symmetric, but the damping matrices $\mathbf{B}^r$, due to the rotating Winkler suspension of the upper roll, are neither symmetric nor anti-symmetric. Both, $\mathbf{B}$ and $\mathbf{B}^r$, are sums of several contributions $\mathbf{B}_k, \mathbf{B}_k^r$. From the Winkler suspension (upper roll) follow

$$\mathbf{B}_1=\pi R B_\psi \tilde{\mathbf{K}}_7,\ \mathbf{B}_2=\pi R B_r \tilde{\mathbf{K}}_8, \tag{A.2.11}$$

Table A.2: Nondimensional inertial, gyroscopic and centrifugal coefficients, $\tilde{m}_k(i,j), \tilde{g}_k(i,j), \tilde{c}_k(i,j)$, of a roll

i,j	$\tilde{m}_1$	*i,j*	$\tilde{g}_1$	*i,j*	$\tilde{m}_2$	*i,j*	$\tilde{m}_2$	*i,j*	$\tilde{g}_2$	*i,j*	$\tilde{c}_2$
1,1	$1+\tilde{a}^2$	9,10	3	2,5	1/2	14,22	-1	7,15	4	6,13	-1
1,4	1	9,23	1	2,12	1/2	15,15	1/2	7,21	9/2	6,19	-3/2
2,2	1	10,24	1	2,20	-1/2	15,21	1	7,22	2	7,7	-6
2,5	1/2	19,20	1	3,6	-1/2	16,16	1/2	8,14	-4	7,14	-4
2,20	1/2	21,22	2	3,13	-1/2	16,24	-3/2	8,21	-2	7,22	9
3,3	1	23,24	3	3,19	-1/2	17,17	1/2	8,22	9/2	8,8	-6
3,6	-1/2			4,4	3	17,23	3/2	9,10	3	8,15	-4
3,19	1/2	*i,j*	$\tilde{c}_1$	4,11	2	19,19	1/2	9,17	6	8,21	-9
4,4	1	4,4	-1	5,5	3/2	20,20	1/2	9,23	19/2	9,9	-27/2
5,5	1/2	5,5	-1	5,12	1	21,21	2	9,24	3	9,16	-9
6,6	1/2	5,20	1	5,20	-1	22,22	2	10,16	-6	9,24	57/2
7,7	1/2	6,6	-1	6,6	3/2	23,23	9/2	10,23	-3	10,10	-27/2
8,8	1/2	6,19	-1	6,13	1	24,24	9/2	10,24	19/2	10,17	-9
9,9	1/2	7,7	-5/2	6,19	1			11,18	1	10,23	-57/2
10,10	1/2	7,22	2	7,7	3/2	*i,j*	$\tilde{g}_2$	12,13	1	12,12	-1/2
18,18	1	8,8	-5/2	7,14	1	1,18	2	12,19	3/2	12,20	1
19,19	1/2	8,21	-2	7,22	-2	2,6	1/2	13,20	3/2	13,13	-1/2
20,20	1/2	9,9	-5	8,8	3/2	2,13	1/2	14,15	2	13,19	-1
21,21	1/2	9,24	3	8,15	1	2,19	1/2	14,21	9/2	14,14	-2
22,22	1/2	10,10	-5	8,21	2	3,5	1/2	15,22	9/2	14,22	5
23,23	1/2	10,23	-3	9,9	3/2	3,12	1/2	16,17	3	15,15	-2
24,24	1/2	18,18	-1	9,16	1	3,20	-1/2	16,23	19/2	15,21	-5
		19,19	-1	9,24	-3	4,18	1	17,24	19/2	16,16	-9/2
i,j	$\tilde{g}_1$	20,20	-1	10,10	3/2	5,3	-1/2	19,20	2	16,24	15
1,18	2	21,21	-5/2	10,17	1	5,6	1	21,22	10	17,17	-9/2
4,18	2	22,22	-5/2	10,23	3	5,13	2	23,24	30	17,23	-15
5,6	1	23,23	-5	11,11	1	5,19	3/2			19,19	-3/2
5,19	1	24,24	-5	12,12	1/2	5,20	1	*i,j*	$\tilde{c}_2$	20,20	-3/2
6,20	1			12,20	-1/2	6,12	-2	5,5	-3/2	21,21	-12
7,8	2	*i,j*	$\tilde{m}_2$	13,13	1/2	6,19	-1	5,12	-1	22,22	-12
7,21	1	1,4	3	13,19	1/2	6,20	3/2	5,20	3/2	23,23	-99/2
8,22	1	1,11	2	14,14	1/2	7,8	2	6,6	-3/2	24,24	-99/2

where $\tilde{\mathbf{K}}_7, \tilde{\mathbf{K}}_8$ are taken from $(A.2.6)_{3,4}$, and the matrices $\mathbf{B}_1^r, \mathbf{B}_2^r$ with

$$\mathbf{B}_1^r = \pi R B_\psi \tilde{\mathbf{B}}_1^r, \ \mathbf{B}_2^r = \pi R B_r \tilde{\mathbf{B}}_2^r, \tag{A.2.12}$$

the elements $b_k^r(i,j)$ of the non-dimensional matrices $\mathbf{B}_k^r, k=1,2$, are listed in Table A.3.

Table A.3: Nondimensional dampings $\tilde{b}_k^r(i,j), k=1,2,$

i,j	$\tilde{b}_1^r$	i,j	$\tilde{b}_1^r$	i,j	$\tilde{b}_1^r$	i,j	$\tilde{b}_2^r$	i,j	$\tilde{b}_2^r$	i,j	$\tilde{b}_2^r$
4,18	2	7,8	2	9,23	1	18,4	-2	21,7	-1	23,24	3
5,6	1	7,21	1	10,9	-3	19,5	-1	21,22	2	24,10	-1
5,19	1	8,7	-2	10,24	1	19,20	1	22,8	-1	24,23	-3
6,5	-1	8,22	1			20,6	-1	22,21	-2		
6,20	1	9,10	3			20,19	-1	23,9	-1		

From (A.1.29) follow – for upper and lower roll – the matrices $\mathbf{B}_3$ and $\mathbf{B}_4$, $\mathbf{B}_5$, respectively, with

$$
\begin{aligned}
&b_3(2,2)=b_{x2}, b_3(3,3)=b_{y2};\ b_4(2,2)=b_{x1}, b_4(3,3)=b_{y1}, b_4(4,4)=b_T/R_1^2,\\
&\mathbf{B}_5=\sum_{l=1}^{3} b_{Sl}\,\mathbf{d}(\alpha_l)\,\mathbf{d}^T(\alpha_l),
\end{aligned}
\tag{A.2.13}
$$

cf. (A.2.4), (A.2.5) for the dyadic products in the last line.

A.2.5 Static Forces

Static we call those forces which arise from the adjustments, cf. Sect. 2.1, preloads and weights. They follow from (A.1.17/18/19) and (A.1.21); cf. (2.14).

In **Aa** are **a** the adjustments given by (2.16) and the non-vanishing elements $A(i,j)$ of the 48×11 matrix **A** read, partly in Matlab notation,

$$
\begin{aligned}
&A(1,1)\ =k_{x1},\ A(2,2)\ =k_{y1},\ A(3,3)\ =k_T/R_1^2,\ A(24,11)=-1/R_2,\\
&A(25,7)=k_{x2},\ A(26,8)=k_{y2},\ A(48,9)=-1,\qquad A(48,10)=1,\\
&\mathbf{A}(17:23,3+l)=k_{Sl}\,\mathbf{d}_l(18:24),\ l=1,2,3.
\end{aligned}
\tag{A.2.14}
$$

The non-vanishing elements of the weight forces $\mathbf{f}_w$ read

$$
\begin{aligned}
&f_w(2)\ =-(m_{H1}+m_{R1})\,g,\qquad f_w(5)\ =0.5\,m_{R1}\,g\,(1+\tilde{a}_1^2/3),\ f_w(12)=m_{R1}g\,\tilde{a}_1^2/6,\\
&f_w(18)=-0.5\,m_{R1}\,g\,(1-\tilde{a}_1^2/3), f_w(26)=(m_{H2}+m_{R2})\,g,\qquad f_w(29)=-0.5\,m_{R2}\,g\,(1+\tilde{a}_2^2/3),\\
&f_w(36)=-m_{R2}\,g\,\tilde{a}_2^2/6,\qquad f_w(42)=0.5\,m_{R1}\,g\,(1-\tilde{a}_2^2/3).
\end{aligned}
\tag{A.2.15}
$$

Appendix A.3: Expansion Coefficients for the Geometrical and Kinematical Relations at the Nip

The non-vanishing elements of the row matrices $\mathbf{s}_{jk}$, $\mathbf{h}_{jk}$ of the nip's shape equations (3.7) read

$$
\begin{aligned}
&s_{20}(4)=s_{20}(5)=s_{20}(7)=s_{20}(9)=1+\tilde{a},\ s_{20}(11)=s_{20}(12)=s_{20}(14)=s_{20}(16)=\tilde{a},\\
&s_{20}(20)=-\tilde{a}, s_{20}(22)=-2\tilde{a}, s_{20}(24)=-3\tilde{a},
\end{aligned}
\tag{A.3.1}
$$

$$
\begin{aligned}
&s_{31}(6)=1+\tilde{a},\ s_{31}(8)=2(1+\tilde{a}),\ s_{31}(10)=3(1+\tilde{a}),\ s_{31}(13)=\tilde{a},\ s_{31}(15)=2\tilde{a},\ s_{31}(17)=3\tilde{a},\\
&s_{31}(18)=1,\ s_{31}(19)=1+\tilde{a},\ s_{31}(21)=1+4\tilde{a},\ s_{31}(23)=1+9\tilde{a},
\end{aligned}
\tag{A.3.2}
$$

$$
h_{10}(18)=h_{10}(19)=h_{10}(21)=h_{10}(23)=1,
\tag{A.3.3}
$$

$$h_{21}(4)=h_{21}(5)=h_{21}(7)=h_{21}(9)=-(1+\tilde{a}),\ h_{21}(11)=h_{21}(12)=h_{21}(14)=h_{21}(16)=-\tilde{a},$$
$$h_{21}(20)=1+\tilde{a},\ h_{21}(22)=2(1+\tilde{a}),\ h_{21}(24)=3(1+\tilde{a}). \tag{A.3.4}$$

The non-vanishing elements of the row matrices $\mathbf{v}_{xjk}$, $\mathbf{v}_{yjk}$ of the velocities (3.8) read

$$\mathbf{v}_{x20}=\mathbf{s}_{20},\ \mathbf{v}_{x31}=\mathbf{s}_{31},$$
$$v_{x30}(6)=1,\ v_{x30}(8)=2,\ v_{x30}(10)=3,\ v_{x30}(18)=v_{x30}(19)=v_{x30}(21)=v_{x30}(23)=1, \tag{A.3.5}$$

$$\mathbf{v}_{y10}=\mathbf{h}_{10},\ \mathbf{v}_{y20}=\mathbf{v}_{y21}=\mathbf{h}_{21}, \tag{A.3.6}$$

$$v_{y31}(6)=-(2+\tilde{a}),\ v_{y31}(8)=-2(2+\tilde{a}),\ v_{y31}(10)=-3(2+\tilde{a}),\ v_{y31}(13)=-\tilde{a},\ v_{y31}(15)=-2\tilde{a},$$
$$v_{y31}(17)=-3\tilde{a},\ v_{y31}(18)=-1,\ v_{y31}(19)=-(2+\tilde{a}),\ v_{y31}(21)=-(5+4\tilde{a}),\ v_{y31}(23)=-(10+9\tilde{a}), \tag{A.3.7}$$

$$v_{y32}(6)=-(1+\tilde{a}),\ v_{y32}(8)=-2(1+\tilde{a}),\ v_{y32}(10)=-3(1+\tilde{a}),\ v_{y32}(13)=-\tilde{a},$$
$$v_{y32}(15)=-2\tilde{a},\ v_{y32}(17)=-3\tilde{a},\ v_{y32}(18)=-1/2,\ v_{y32}(19)=-(1+\tilde{a}), \tag{A.3.8}$$
$$v_{y32}(21)=-(5+8\tilde{a})/2,\ v_{y32}(23)=-(5+9\tilde{a}).$$

The non-vanishing elements of the row matrices $\mathbf{k}_{xjk}$, $\mathbf{k}_{yjk}$ of the virtual displacements (3.9) read

$$\mathbf{k}_{x00}=\mathbf{s}_{20},\ \mathbf{k}_{x11}=\mathbf{s}_{31}, \tag{A.3.9}$$

$$k_{x22}(4)=-(1+\tilde{a})/2,\ k_{x22}(5)=-(1+\tilde{a}),\ k_{x22}(7)=-5(1+\tilde{a})/2,\ k_{x22}(9)=-5(1+\tilde{a}),$$
$$k_{x22}(11)=-\tilde{a}/2,\ k_{x22}(12)=-\tilde{a},\ k_{x22}(14)=-5\tilde{a}/2,\ k_{x22}(16)=-5\tilde{a},\ k_{x22}(20)=1+\tilde{a}, \tag{A.3.10}$$
$$k_{x22}(22)=2+5\tilde{a},\ k_{x22}(24)=3(1+5\tilde{a}),$$

$$\mathbf{k}_{y00}=\mathbf{h}_{10},\ \mathbf{k}_{y11}=\mathbf{h}_{21},\ \mathbf{k}_{y22}=\mathbf{v}_{y32}. \tag{A.3.11}$$

Appendix A.4: Numerical Values of the System Parameters

The Tables A.4 to A.7 list the chosen numerical values of the basic system parameters (rounded), cf. Sect. 4.2:

Table A.4: General parameters

$b = 1$ m	$g = 9.81$ m/s^2	$E = 2.10 \cdot 10^{11}$ N/m^2	$\nu = 0.3$	$\rho = 7850$ kg/m^3	$\Omega_N = 72.25$ rad/s

Table A.5: Parameters of roll 1

$R_1 = 310$ mm	$k_{S1} = 7.42 \cdot 10^7$ N/m	$b_{x1} = 193$ Ns/m	$a_{x1} = 0.0155$ mm
$a_1 = 36$ mm	$\alpha_1 = 0$	$b_{y1} = 278$ Ns/m	$a_{y1} = 2.93$ mm
$m_{H1} = 986$ kg	$k_{S2} = 7.42 \cdot 10^7$ N/m	$b_T = 6.35$ Nms/rad	$a_{S1} = -0.847$ mm
$k_{x1} = 5.15 \cdot 10^7$ N/m	$\alpha_2 = 0.524$ rad	$b_{S1} = 222$ Ns/m	$a_{S2} = -2.91$ µm
$k_{y1} = 7.42 \cdot 10^7$ N/m	$k_{S3} = 7.42 \cdot 10^7$ N/m	$b_{S2} = 222$ Ns/m	$a_{S3} = -2.91$ µm
$k_T = 1.69 \cdot 10^6$ Nm/rad	$\alpha_3 = -0.524$ rad	$b_{S3} = 222$ Ns/m	$\varphi_{N0} = 4.72 \cdot 10^{-4}$ rad

Table A.6: Parameters of roll 2

$R_2 = 420$ mm	$k_{x2} = 1.06 \cdot 10^8$ N/m	$b_{x2} = 396$ Ns/m	$a_{x2} = -1.90$ µm
$a_2 = 66$ mm	$k_{y2} = 1.52 \cdot 10^8$ N/m	$b_{y2} = 570$ Ns/m	$a_{y2} = 0.146$ mm
$m_{H2} = 1540$ kg	$K_r = 2.10 \cdot 10^{10}$ N/m^2	$B_r = 6.30 \cdot$Ns/m^2	$M_r = 97.2$ N m
$J_2 = 48.20$ kg m^2	$K_\psi = 8.08 \cdot 10^9$ N/m^2	$B_\psi = 2.42 \cdot 104$ Ns/m^2	

Table A.7: Parameters of the paper: Nominal speed $v_P = 25$ m/s

$H_1 = 0.15$ mm	$F_1 = 900$ N	$\varepsilon_l = 0.13$	$\mu_{01} = 0.30$
$L_1 = 1$ m	$F_2 = 300$ N	$\varepsilon_{ul} = 0.045$	$v_{c1} = 0.1$ mm/s
$L_2 = 1$ m	$E_l = 4.60 \cdot 10^6$ N/m^2	$b_p = 5.0 \cdot 10^{-5}$ s	$\mu_{02} = 0.25$
$m_P = 0.20$ kg	$E_{ul} = 6.80 \cdot 10^6$ N/m^2		$v_{c2} = 0.1$ mm/s

References

Brommundt, E.: A simple model for friction induced high-frequency self-excitation of paper calenders. *Machine Dynamics Problems* 31 (2007), 25 – 45

Brommundt, E.: High-order sub-harmonic synchronization in a rotor system with a gear coupling. *Technische Mechanik*, 24, (2004), 242 – 253

Brommundt, E.: Ein Reibschwinger mit Selbsterregung ohne fallende Reibkennlinie. *Zeitschrift für angewandte Mathematik und Mechanik*, ZAMM 75, (1995), 811 – 820

Brommundt, E.: Wechselwirkungen zwischen Polygonalisation und Antrieb bei Eisenbahnrädern. *Technische Mechanik*, 16 (1996), 273 – 284

Bullo, F., Lewis, A. D.: Geometric Control of Mechanical Systems. Text in *Applied Mathematics*, Vol. 49, Springer Science+Buisiness Media, Inc. (2005)

Fleischer, G., Gröger, H., Thum, H.: *Verschleiß und Zuberlässigkeit*. VEB Verlag Technik, Berlin 1980

van Haag, R.: Über die Druckspannungsverteilung und die Papierkompression im Walzenspalt eines Kalan-ders. Dissertation, Darmstadt, D 17, 1993

Hader, P.:Selbsterregte Schwingungen von Papierkalandern. Dissertation, Duisburg-Essen. Shaker Verlag, Aachen (2005).

Kovriguine, D. A., Potapov, A. I.: Nonlinear oscillations of a thin ring. – I. Three-wave resonant interactions. *Acta Mechanica* 126, (1998), 189 – 200.

Kovriguine, D. A.: Nonlinear oscillations of a thin ring. – II. Four-Wave resonant interactions. Self-modulation. *Acta Mechanica* 126, (1998), 201 – 212.

Shelley, S., Zwart, J., Fournier, A.: New insights into calender barring prevention. 83rd Annual Meeting, Technical Section, CPPA, January (1997), 1 – 8.

Roisum, D., R.: *The Mechanics of Rollers*, Tappi Press, Atlanta, GA, 1996, 1998

Washizu, K. *Variational Methods in Elasticity and Plasticity*; 3rd Edition. Pergamon Press, Oxford etc. (1982).

Address: Prof. em. Dr. Eberhard Brommundt, Institut für Dynamik und Schwingungen, Technische Universität Braunschweig, PF 3329, D-38023 Braunschweig.

e-mail, priv.: Eberhard@Brommundt.de, TU: E.Brommundt@tu-braunschweig.de